Hysteresis and dynamics compensation for accurate positioning in high speed piezo scanning stages

Steinbusch, A.J.J.

Award date:
2020

Department of Mechanical Engineering

Dynamics & Control

DC 2020.056

Hysteresis and Dynamics Compensation for Accurate Positioning in High Speed Piezo Scanning Stages

Master's Thesis Report

Author:

A.J.J. Steinbusch *(0903892)*
a.j.j.steinbusch@student.tue.nl

Supervisors:

dr. H. Sadeghian
h.sadeghian.marnani@tue.nl

prof. dr. H. Nijmeijer
h.nijmeijer@tue.nl

Eindhoven

4th June, 2020

Abstract

New advancements in nanotechnology applications demand higher bandwidth actuation of high-speed piezo scanning stages while maintaining high positioning accuracy. However, hysteresis and vibrational dynamics make accurate positioning of these systems at high bandwidth a challenging task. While most work focuses on compensating either hysteresis or dynamics in order to improve positioning accuracy, a proper and comprehensive dynamic framework that is able to compensate for both hysteresis and vibrational dynamics at high bandwidth is still missing. In this thesis, a modeling framework is proposed that is able to describe the full dynamics of high speed piezo scanning stages by modeling the hysteresis and vibrational dynamics together. Then, the approach is experimentally applied to a miniaturized high-speed piezo-actuated scanning stage. Experimental results demonstrate that the proposed modeling framework is able to describe the amplitude and frequency varying dynamics of the scanning stage with less than 1% RMS error for the full actuation bandwidth. The results presented in this work can be used for improved model-based feed-forward control combined with feedback control in order to improve the positioning accuracy of high speed scanning stages.

Contents

Chapter 1

Introduction

Nanotechnology is all about understanding and controlling matter at dimensions less than 100nm [1]. An important aspect of this research field is precision control and manipulation at nanoscale. This is called nanopositioning. Nanopositioning systems are built to move objects over a very small distance, with resolutions down to atomic level. These systems are generally driven by piezoelectric actuators and have been widely applied in high-precision systems such as micromanipulator and ultra-precision machine tools [2].

Piezo-actuated nanopositioning stages also play a key role in atomic force microscopy (AFM) [3], which is a type of scanning probe microscopy (SPM) [1]. An AFM utilizes a micro cantilever with a small tip to "feel" the topology of a sample, as shown in Figure 1.1. The tip of the cantilever is able to sense the forces that are being exerted on it by the atoms in the sample that is being scanned. The forces acting on the cantilever tip influence the deflection of the cantilever. An Optical Beam Deflection (OBD) measurement system is used to measure this deflection. A feedback loop is used to control a nanopositioning stage (the z-stage) in vertical direction with the purpose of keeping the cantilever tip at the most sensitive position. The topology of the surface can be reconstructed using the OBD measurements and the control voltage that is sent to the z-stage. The bandwidth of the z-stage is often the limiting factor for the scanning speeds that can be achieved using these systems [4].

Numerous research areas and industrial applications have been fundamentally changed with the development of nanopositioning systems, including biology, chemistry, material science [5] and high density data storage systems [6]. Currently, lots of new potential

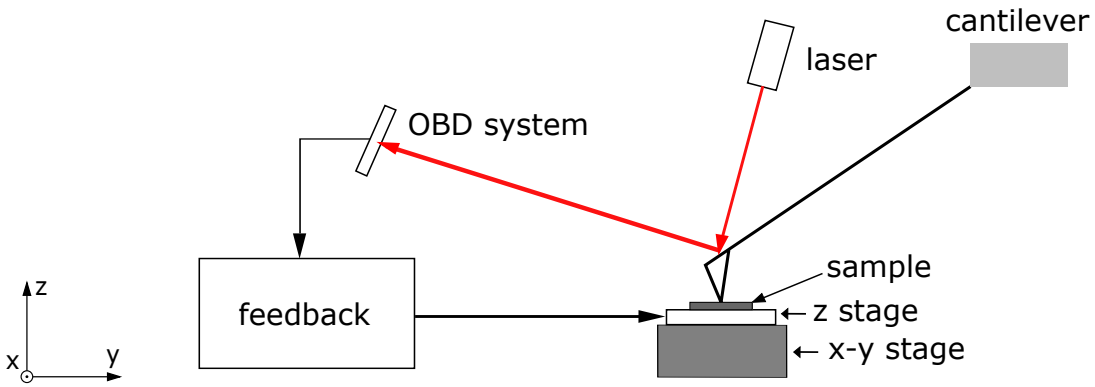

Figure 1.1 Schematic representation of an AFM system. The deflection of the cantilever is being measured via a laser by the OBD system as the x-y stage moves the sample relative to the cantilever tip. This data is used to control the position of the z-stage using a feedback controller.

applications require higher bandwidth actuation of systems such as the AFM while maintaining high positioning accuracy. Examples include subsurface scanning probe microscopy [7], the study of the fast dynamic movement of biological cells in real time [3] and wafer metrology in semiconductor applications [8]. In order to meet this demand, high-speed nanopositioning stages are being developed that can be actuated at much higher bandwidth [8, 9]. The positioning errors in these systems are mainly caused by hysteresis that is inherently present within piezo-actuated systems and dynamics as a result of the characteristics of the mechanical stage [1, 2].

1.1 Hysteresis

Piezoelectric materials suffer from a nonlinearity between the applied voltage and the obtained displacement, referred to as hysteresis. In order to more clearly reveal the impact of this nonlinearity, an oscillating voltage can be applied to a piezo-actuated stage. Due to hysteresis, the displacement does not travel along the same path when the voltage is decreased after it is initially increased. This results in a so-called hysteresis loop between input and output, shown in Figure 1.2. The output displacement is not only dependent on the current input voltage, but also on previous input voltages. This is a memory effect referred to as non-local memoryless [10, 11], which results in amplitude-dependent behaviour [2]. This hysteresis phenomenon creates nonlinearities in the constitutive relations between input fields E and stresses σ, and output polarisation P and strains ϵ in the piezoelectric material [12].

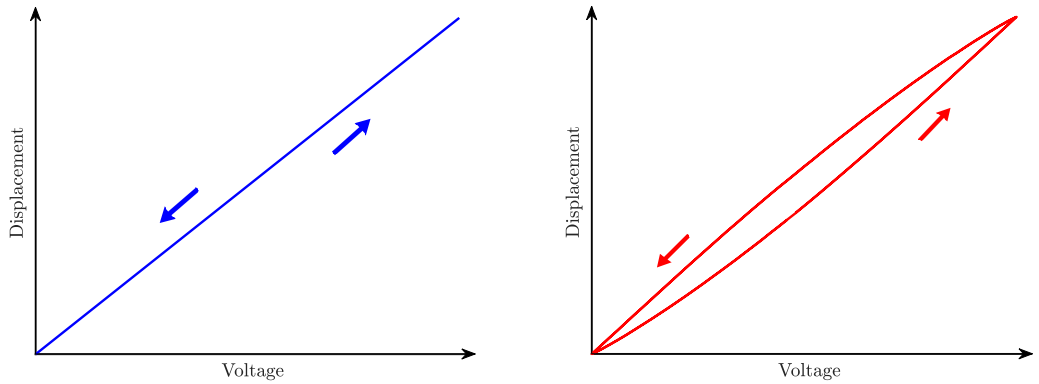

(a) Linear voltage-to-displacement behaviour without hysteresis

(b) Observed voltage-to-displacement as a result of hysteresis behaviour

Figure 1.2 Illustration of a linear and the actual observed voltage-to-displacement behaviour in a piezoelectric actuator when an oscillating voltage is applied. The observed voltage-to-displacement behaviour on the right side is known to as the hysteresis phenomenon. Arrows indicate the direction of the path that is described.

1.2 Vibrational Dynamics

Besides hysteresis, vibrational dynamics as a result of the structural characteristics of scanning stages is a major bottleneck in achieving high accuracy at high speeds for nanopositioning [13]. Piezo-actuated stages are typically characterized by high stiffness and low structural damping, which leads to a "sharp", lightly damped resonance peak in its frequency response [2]. Input signals that contain high-frequency components excite this resonance and induce vibrational effects which negatively affect the positioning accuracy, of which an example is shown in Figure 1.3. This disturbance is often avoided by highly limiting the operating bandwidth of piezo-actuated stages to approximately 1% of the first resonance frequency [13]. However, this will result in drastically limiting the speed, which means that this is not a plausible solution for high speed stages.

1.3 Control Strategies & Issues

Compensating hysteresis and vibrational dynamics in high speed piezo scanning stages could be achieved by feedback control with sufficiently high feedback gain. However, the improvements that can be achieved in terms of positioning accuracy are limited because of the typically low gain margins of these systems as a result of the "sharp", lightly damped resonant peak and phase loss due to filters and other high-frequency dynamics [1]. Additionally, it is reported [14] that hysteresis reduces the gain and

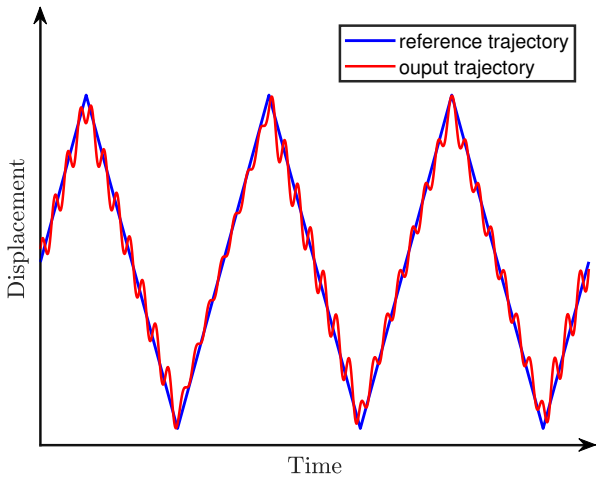

Figure 1.3 Illustration of uncompensated vibrational dynamics excited by high-frequency components in the actuation voltage causing oscillations during open loop tracking

phase margins of these systems in closed loop even further, up to 28%. This quickly leads to an unstable feedback system which limits the operating bandwidth that can be achieved using feedback control [2, 12, 13].

In addition to feedback control, feed-forward control can theoretically improve the accuracy of piezo scanning stages by exploiting a priori knowledge of the system's hysteresis and vibrational dynamics. This control approach does not suffer from the issues associated with feedback control and can therefore improve the accuracy, even at high operating speeds [1]. Several attempts are being made on compensating hysteresis and dynamics of nanopositioning systems by developing feed-forward controllers based on inverse models that improve the performance of these systems [15, 12, 16, 17]. The main focus of most feed-forward control approaches has been on compensating either hysteresis or vibrational dynamics.

For hysteresis compensation [18, 19, 20, 21], inverted hysteresis models are utilized that describe the hysteresis nonlinearity phenomenologically [2]. Examples of these models include the Preisach model [22], the Krasnosel'skii-Pokrovkii model [12], the Prandtl-Ishlinskii model [23], the Bouc-Wen model [24] and the Maxwell model [25, 26]. Dynamic effects that are observed are often referred as rate-dependent hysteresis [2]. Existing mathematical models are often modified to capture this rate-dependency [27, 28, 18, 29, 30]. However, due to the introduction of time-derivatives of input or output signals, these models tempt to become very complex for model identification and

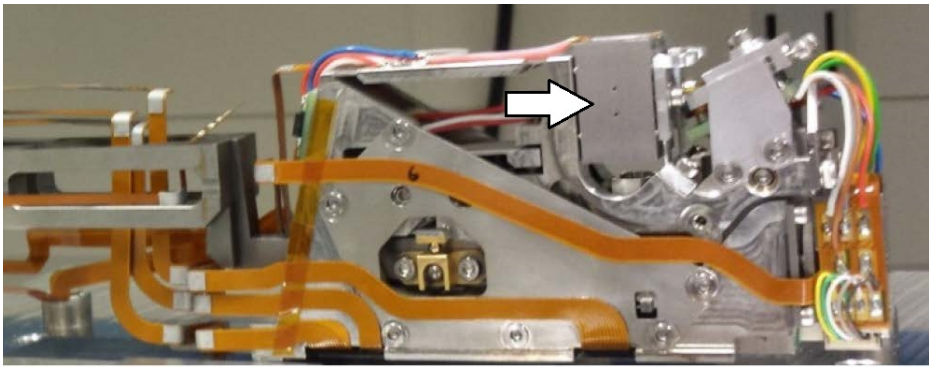

Figure 1.4 Photo of the miniaturised AFM developed [5] for high-throughput parallel AFM [9] showing the high speed scanning stage in use, highlighted by the arrow.

noise amplification problems may occur when used in inverse model-based feed-forward controllers [2]. This makes these rate-dependent models unfavorable for model-based feed-forward control for high speed piezo stages. An alternative approach that almost fully eliminates the need for hysteresis compensation is using a charge drive rather than a voltage drive. However, this method is rarely used for controlling piezo-actuated systems because of its high cost and implementation complexity [2].

Alternatively, rather than compensating hysteresis, some works focus on compensating the vibrational dynamics in order to the improve positioning accuracy of these systems. Examples include input shaping control [31] and the optimal-inversion based approach [32]. Amplitude varying dynamics in such control approaches as a result of hysteresis can be avoided by using low voltage amplitude actuation [33].

Finally, attempts are being made on compensating both hysteresis and vibrational dynamics in a feed-forward setting [15, 16]. Existing techniques for hysteresis and vibration compensation such as inverse mathematical hysteresis models [2] and the optimal-inversion based approach [32] are often combined in an attempt to successfully compensate for both error sources.

In order to successfully implement such a compensation in high-speed piezo scanning stages, a framework is required that allows to compensate for both rate-dependent and amplitude-dependent dynamics as a result of the coupled [2] hysteresis and dynamic behaviour. Model-based feed-forward control can fulfill a major role in achieving this. However, this requires a modeling framework that describes the full dynamics of the system with high accuracy up-to the full bandwidth of actuation.

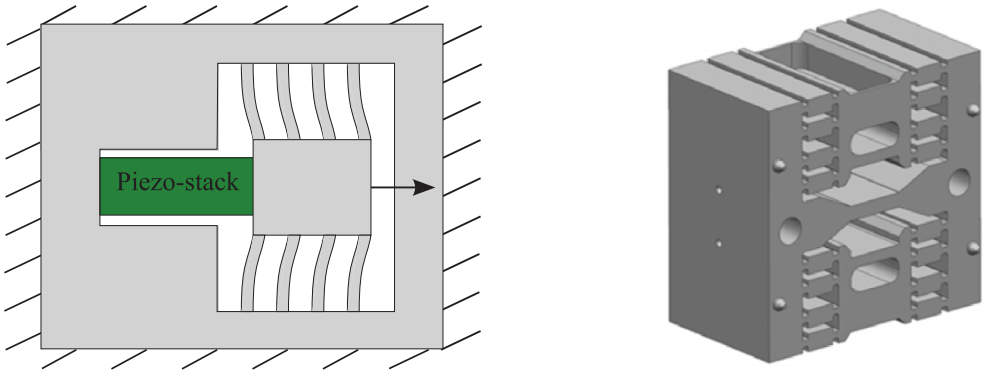

(a) Flexure-guided piezo-stack actuator [3] **(b)** Miniaturised z-stage [8]

Figure 1.5 (a) Illustration of the flexure guided piezo-stack actuator that is used in the high-speed scanning stage shown in (b)

The goal of this thesis is to formulate and experimentally validate such a modeling framework. The formulation of this framework specifically aims at accurately describing the amplitude and frequency varying behaviour of high speed piezo scanning stages as a result of hysteresis and dynamics.

The formulation of such a modeling framework contributes to the improvement of feed-forward control for high speed scanning stages. A feed-forward based on the formulated modeling framework can, in addition to feedback control, be used to improve the positioning accuracy of high speed scanning stages at high bandwidth.

1.4 Scope of This Work

In this thesis, the work [15, 16] on compensating both hysteresis and dynamics in piezo-actuated stages is continued by proposing a modeling framework for describing rate-dependent and rate-independent hysteresis as well as the vibrational dynamics of high speed piezo-actuated scanning stages, supported by experimental results. The proposed framework deals with the rate-dependent hysteresis by capturing the rate-dependent effects and the vibrational dynamics within one linear model. This model is split into two sub-models in order to achieve this. Additionally, the hysteresis nonlinearity is described by a nonlinear rate-independent model. This approach is experimentally applied to a miniaturized [5] high-speed piezo-actuated scanning stage [8], which has its first resonance at about 50kHz. The stage is used in the AFM scan head shown in Figure 1.4 for high-speed positioning of the cantilever with respect to the sample during scanning [8] in high-throughput parallel AFM [9]. The high-speed

scanning stage indicated in Figure 1.4 is shown up-close in Figure 1.5.

The outline of this thesis is ordered as follows. First, the experimental setup that is used for this work is presented in Chapter 2. In Chapter 3, a modeling framework is proposed and formulated for characterizing the hysteresis behaviour and vibrational dynamics of high speed scanning stages. Chapter 4 explains the model identification that is performed when applying the proposed modeling framework to the high speed scanning stage considered in this work. Finally, the identified model is validated in Chapter 5 by comparing predicted model output displacements with experimentally measured displacements for frequency and amplitude varying actuation voltages, showing that both dependencies are captured within the model.

Chapter 2

Experimental Setup

An experimental setup is used to perform the research in this work. This chapter explains the architecture of the setup, the components that are used and the most important specifications of these components. A photo of the setup is shown in Figure 2.1 and the setup architecture is shown schematically in Figure 2.2. In Table 2.1, a summary of the components and the most important specifications is presented.

The scanning stage used in the setup utilizes a flexure-guided mechanism driven by a piezo-stack actuator, similar to that of the miniaturized [5] high-speed piezo-actuated scanning stage [8] shown in Figure 1.5. The stage is shown up-close in the inset in Figure 2.1. The PI-883.11 piezo element used in the scanning stage has a capacitance of 210nF, a maximum travel range of 8μm and can be driven up-to 100V. The maximum peak-to-peak excitation voltage that is used in this work is limited to 80V as a safety measure. The setup utilizes a PiezoDrive PDu 150V high voltage amplifier with a gain of 20 for driving the scanning stage. The amplifier has a power bandwidth of up-to 80kHz, depending on the capacitive load of the piezo and the peak-to-peak voltage stroke that is applied. This selection of piezo capacitance and high voltage amplifier allows the stage to be driven up to its resonance frequency, which is located at approximately 20kHz [34]. However, the actuation of the stage may be affected by the amplifier bandwidth at higher operating frequencies as a result of the piezo capacitance and the applied voltage stroke, which must be considered when interpreting experimental data.

The displacement of the scanning stage is measured using a Polytec VibroFlex laser vibrometer utilizing a VibroFlex Fiber sensor head, which allows for fast and accurate

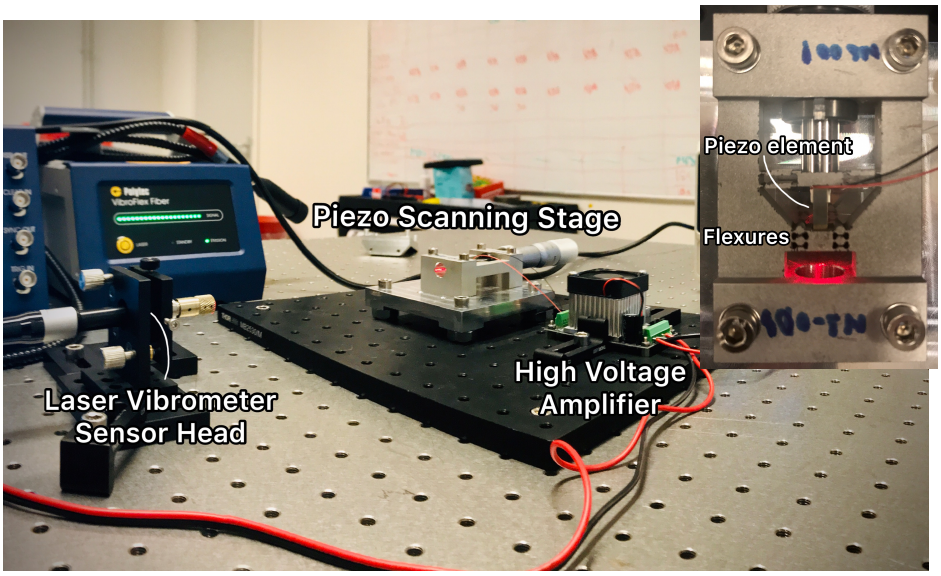

Figure 2.1 Photo of the experimental setup that is referred to throughout this work, the inset shows an up-close top view of the scanning stage.

measuring with a bandwidth of up-to 24MHz and a resolution down-to 0.1pm/Hz$^{0.5}$. A selected bandwidth of 500kHz is used for the experiments performed in this work, with a measurement sensitivity of 2.5μm/V. The software design on the host PC combined with the NI-PCI-6229 DAQ device and BNC-2110 (16 bit) allows for synchronous data acquisition and signal generation at sample rates up-to 250kHz. Synchronous data acquisition is used in order to prevent delay between input and output signals as a result of signal processing. With a measurement sensitivity of 2.5μm/V and a signal output of 0-2V, the 16-bit resolution of the DAQ allows for a measurement resolution of 0.15nm, which is a typical requirement for nanopositioning stages. The available sample rate is sufficient for measuring the resonance of the scanning stage at approximately 20kHz. The selection of this displacement sensor and DAQ device allows for sub-nm resolution displacement measurements at a bandwidth that allows for measuring the resonance of the scanning stage.

With this, the setup that is used for the research in this work is presented. The setup architecture allows for actuating the high speed stage up-to its resonance at approximately 20kHz while measuring with sub nanometer level resolution. More details on the individual components are listed in Table 2.1. The development of this setup and more details on specifications are discussed more extensively in [34].

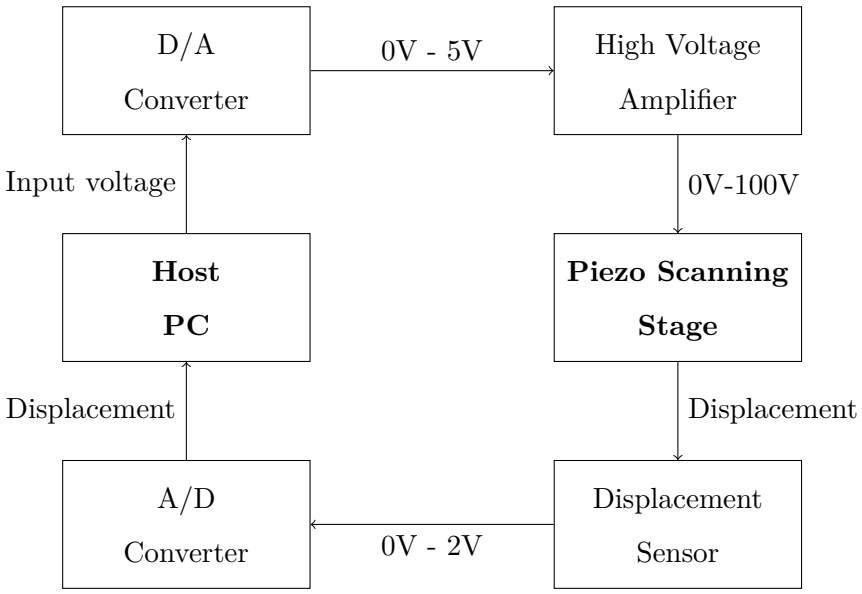

Figure 2.2 Schematic representation of the architecture of the experimental setup shown in Figure 2.1, details on components are given in Table 2.1.

Table 2.1 List of components of the experimental setup and their specifications

	Component	**Specifications**
A/D + D/A Converter	NI-PCI-6229 with NI-BNC-2110	Resolution: 16-bit Sample rate: 250kHz voltage range: ±10V
High Voltage Amplifier	PiezoDrive, PDu 150V	Bandwidth: 80kHz @2V Noise: 36μV@100nF
Piezo Element	PI-883.11	Capacitance: 210nF Bandwidth: 135kHz Stiffness: 36N/μm max. travel range: 8μm
Displacement Sensor	Polytec VibroFlex Laser Vibrometer	freq. range: up-to 24MHz Resolution: 0.1pm/Hz$^{0.5}$ Max. displ.: 0.01μm-2.5m

Chapter 3

Model Formulation

In this chapter, a modeling framework is proposed and formulated for predicting the output displacement of a piezo-actuated high speed scanning stage for a given input voltage. For this, the hysteresis nonlinearity in the piezo-actuator of the stage and the vibrational dynamics of the mechanical stage itself play an important role. The chapter starts with an overview of what the modeling framework must capture, followed by a motivation for the framework that is chosen based on experimental data obtained from the experimental setup presented in Chapter 2. After this, the modeling framework is further formulated and defined in detail.

The modeling framework must be able to accurately predict the output displacement of a piezo-actuated scanning stage over its full actuation bandwidth, taking into account both frequency and amplitude dependent behaviour. For this, it is necessary to model the vibrational dynamics of the stage as well as the hysteresis effect within the piezoelectric actuator. Rate-dependent hysteresis that may be present must be taken into account as well. Including both the vibrational dynamics and the hysteresis nonlinearity allows the modeling framework to capture both the frequency-dependent and amplitude-dependent behaviour, which is a key element in describing the full dynamics of a piezo-actuated high speed scanning stage.

The consequence of hysteresis in piezo-actuated systems is often shown by applying an oscillating voltage to the actuator. Visualizing the obtained voltage-to-displacement behaviour reveals the so-called hysteresis loop. It is claimed that the rate of the applied voltage generally significantly effects the hysteresis loop that is observed [2]. In order to gain more insight in the hysteresis nonlinearity, voltage-to-displacement loops are

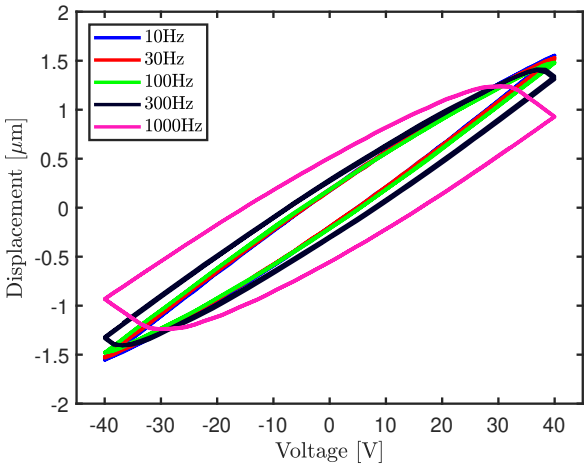

Figure 3.1 Experimentally measured voltage-to-displacement loops using triangular input voltages at various driving frequencies

measured, shown in Figure 3.1. These loops are measured on the setup presented in Chapter 2 using 80V peak-to-peak triangular voltage strokes at different actuation frequencies. A brief overview of the execution of experiments is given in Appendix A.1. It is clear that the output displacement is indeed dependent upon the frequency of actuation. Three main effects are observed as the frequency of actuation is increased:

1. Decreasing loop stiffness;
2. Increasing width;
3. Negative gradients at extremes.

In Figures 3.2a and 3.2b, some of the experimental data is shown in time-domain. The curved path of the normalized output with respect to the input in the 10Hz data in Figure 3.2a reveals the hysteresis phenomenon that is present in the piezo-actuator of the scanning stage. In the 1000Hz data shown in Figure 3.2b, the presence of phase lag between the input and output signals becomes visible, which shows that hysteresis is coupled with additional linear dynamics, as concluded in [15]. A qualitative phase lag compensation is performed in order to further demonstrate the effect of phase lag on the hysteresis loops shown in Figure 3.1. This is done by aligning the input and output extremes in time-domain. The result of this compensation is shown for 10Hz and 1000Hz in Figure 3.2. It shows that linear dynamics and time-delays in the system play a big role in the rate-dependent effects that are observed in so-called hysteresis loops. These effects are likely caused by the mechanical characteristics

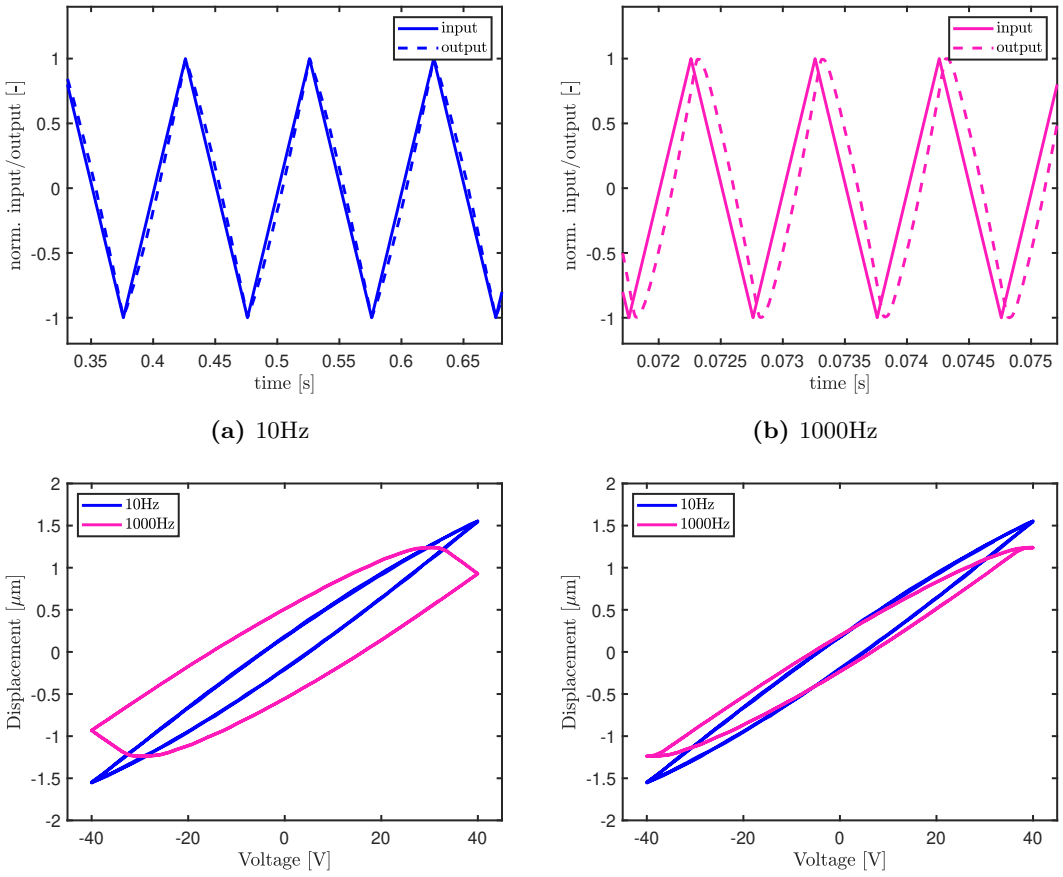

(a) 10Hz

(b) 1000Hz

(c) Measured voltage-to-displacement loops without phase lag compensation

(d) Measured voltage-to-displacement loops with phase lag compensation

Figure 3.2 Normalized input (voltage) and output (displacement) signals revealing the presence of phase lag at increasing frequencies (10Hz, 1000Hz) and an illustration of the effect of a qualitative phase lag compensation on the hysteresis loops at various driving frequencies, using an 80V peak-to-peak voltage stroke. The phase lag compensation is performed by aligning input and output extremes in time-domain.

of the stage, which includes vibrational dynamics, and the electrical characteristics of the voltage amplification circuit. This has been reported before, for example in [15, 16]. This phase lag compensation confirms that hysteresis can be modeled as a rate-independent nonlinearity by distinguishing the effect from linear dynamics and time-delays. Based on this, a modeling framework is proposed for the characterization of the full dynamic behaviour of the piezo-actuated high speed scanning stage, which includes both the hysteresis nonlinearity and the linear vibrational dynamics in the system. The formulation of this framework is explained in Section 3.1.

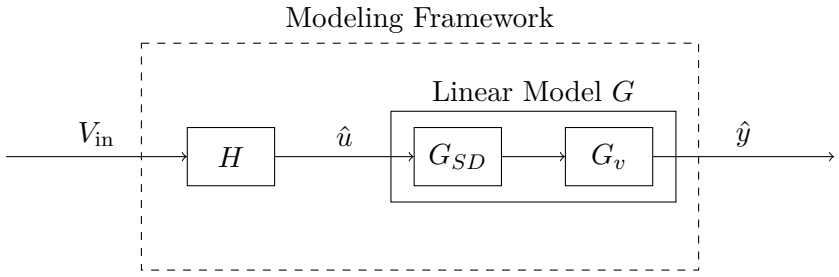

Figure 3.3 Schematic representation of the full modeling framework describing the dynamics of the piezo scanning stage with the input voltage V_{in} and output displacement $\hat{y}$, block H represents the rate-independent hysteresis model and $\hat{u}$ represents the hysteresis model output, block G_{SD} represents the spring-damper sub-model and G_v represents the sub-model that describes the vibrational dynamics. The full linear model is defined as $G = G_{SD}G_v$.

3.1 Modeling Framework

Based on the conclusions drawn from the experimentally obtained data in Figure 3.1, a modeling framework for modeling the full dynamics of the piezo scanning stage is proposed in this section. The experimentally obtained data shows that the observed hysteresis effects are coupled with additional linear dynamics when increasing the actuation frequency. These linear dynamics explain the "rate-dependent hysteresis effects" that are observed. For this reason, the modeling framework that is proposed treats the hysteresis nonlinearity as rate-independent by utilizing a rate-independent hysteresis model H. The hysteresis model H is cascaded with a linear model G. The linear model G is used for describing the vibrational dynamics of the scanning stage. By using this framework, the rate-dependent hysteresis effects and the vibrational dynamics are captured within one linear model.

The proposed framework, shown schematically in Figure 3.3, describes the full input-output behaviour from input voltage V_{in} to output displacement y. The rate-independent hysteresis model H maps the input voltage to an intermediate hysteresis signal $\hat{u}$. The linear model G maps the hysteresis output signal $\hat{u}$ to the model output displacement $\hat{y}$. This modeling framework simplifies the modeling challenges associated with piezo-actuated systems as a result of hysteresis by decoupling the hysteresis nonlinearity and the traditional linear effects, which solves the rate-dependency problem that is often faced in modeling piezo-actuated systems.

The linear model G consists of two sub-models, a spring-damper model G_{SD} and

a vibrational model G_v. The vibrational model G_v captures the traditional linear dynamics of the system, with an emphasis on the vibrational dynamics at high frequency resulting from the mechanical characteristics of the stage. The spring-damper model, also known as the Kelvin-Voight model [16], is often used for modeling creep in piezo-actuators. Creep is often observed at operating frequencies below 1Hz. In this work however, the spring-damper (Kelvin-Voight) model is used to support the vibrational model G_v by capturing all rate-dependent effects which the vibrational model fails to capture. The hysteresis model H captures the rate-independent hysteresis nonlinearity in the actuator. Note that the physical signal $\hat{u}$ cannot be measured directly because hysteresis happens on molecular level in the piezoelectric material. The formulation and identification of the hysteresis model H and the linear model G is discussed in Sections 3.2 and 3.3, respectively.

3.2 Hysteresis Model: Prandtl-Ishlinksii

In this section, the formulation of the hysteresis model H is given. The model that is chosen for this is the well known Prandtl-Ishlinskii (P-I) model [23]. This model is widely used in literature for describing hysteresis in various applications, among which the modeling of hysteresis in piezoelectric actuators [35, 36]. The main motivation for choosing this model is its analytical invertibility, meaning that the inverse of this model is exact and can directly be derived from the forward P-I model, as done in e.g. [36, 37]. This makes this model very favorable for feed-forward control applications. The traditional Prandtl-Ishlinksii model is defined [37] as

$$\hat{u}(t) = a_0 V_{\text{in}}(t) + \int_0^R a(r) F_r[V_{\text{in}}](t) \mathrm{d}r, \tag{3.1}$$

where $\hat{u}(t)$ represents the output of the model and $V_{\text{in}}(t)$ is the input of the model at time t, parameter $a(r)$ represents a density function, a_0 is a positive constant and $F_r[V_{\text{in}}](t)$ is the play operator. For the definition of the play operator [23], let $C_m[0, t_E]$ be the space of piecewise continuous functions. For an input $V_{\text{in}}(t) \in C_m[0, t_E]$, let $0 = t_0 < t_1 < t_2 < \cdots < t_N = t_E$ be a partition of $[0, t_E]$, such that $V_{\text{in}}(t)$ is monotone on each of these sub-intervals $C_m[t_i, t_{i+1}]$. The play operator $F_r[V_{\text{in}}](t)$ is then defined

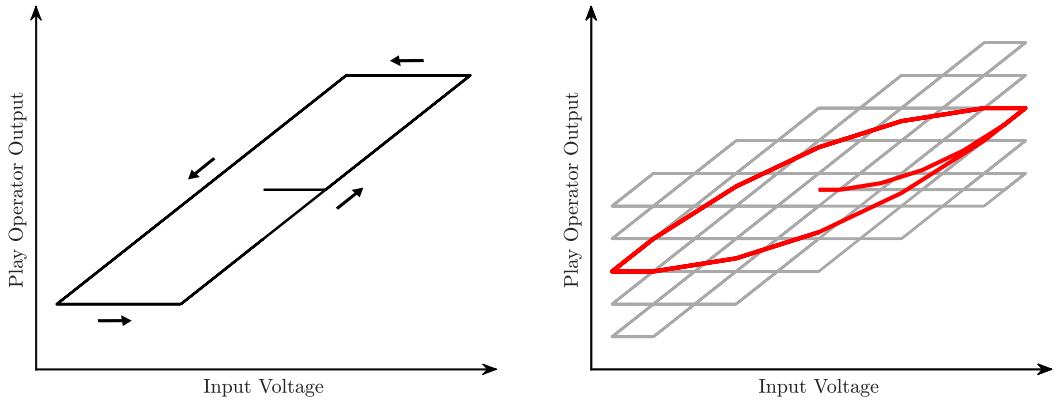

(a) single play-operator **(b)** weighted summation of play-operators

Figure 3.4 Play operator illustration: The left figure illustrates the output of a single play operator with a threshold r as a function of an oscillating input voltage, where the arrows indicate the path of the output of the play operator. The right figure illustrates a weighted summation of multiple play operators with different thresholds r_i (in gray) to obtain a modeled hysteresis loop (in red).

as follows:

$$z(0) = F_r[V_{\text{in}}](0) = f_r(V_{\text{in}}(0), 0), \tag{3.2}$$

$$z(t) = F_r[V_{\text{in}}](t) = f_r(V_{\text{in}}(t), z(t_i)), \tag{3.3}$$

for $t_i < t \leq t_{i+1}$ and $0 \leq i \leq N-1$, with

$$f_r(V_{\text{in}}, z) = \max\left[V_{\text{in}} - r, \min(V_{\text{in}} + r, z)\right], \tag{3.4}$$

where $z(t)$ represents the output of the play operator, shown in Figure 3.4a. The P-I model as described here is used as a base for describing the hysteresis nonlinearity in the piezo-actuated stage. In order to implement the formulated P-I model in real-time, the model formulated in Eq. (3.1) is discretised. At the kth time step, the discretised P-I model is given by

$$\hat{u}(k) = a_0 V_{\text{in}}(k) + \sum_{i=1}^{Q} a_i F_{r_i}\left[V_{\text{in}}(k)\right], \tag{3.5}$$

with $\hat{u}(k) := \hat{u}(t_k)$, where t_k represents the time at the kth time-step. The integral term in Eq. (3.1) is approximated by a sum of Q play operators with discrete thresholds

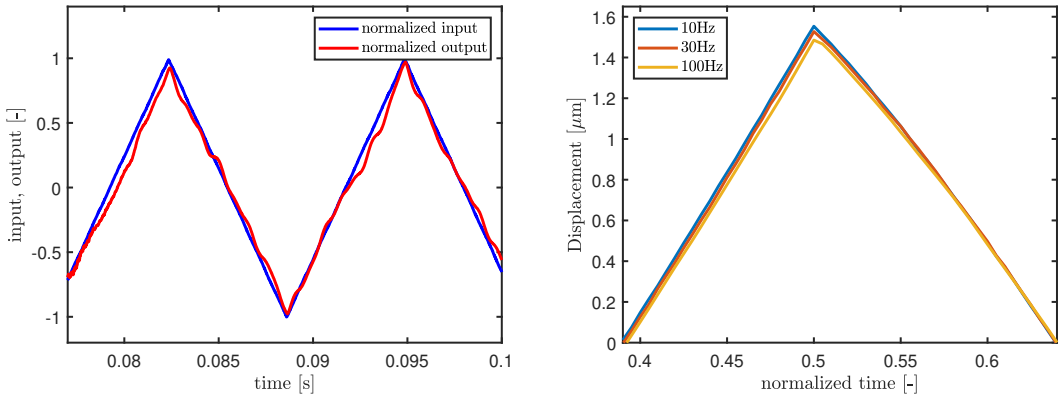

(a) Observed vibration in the output as a result of the mechanical structure of the stage, measured using high frequency triangular input signals

(b) Measured output signals for triangular input signals with different frequencies normalized to time

Figure 3.5 Measured responses of the piezo-actuated scanning stage subjected to triangular input signals showing vibration and additional low-frequency dynamics in the system

r_i. These discrete thresholds r_i are defined as

$$r_i = \frac{i-1}{Q}||V_{\text{in}}(k)||_\infty \quad \text{for} \quad i = 1, 2, \ldots, Q. \tag{3.6}$$

The outputs of the play operators $F_{r_i}[V_{\text{in}}(k)]$ are multiplied by weights a_i, which replace the continuous density function $a(r)$ in Eq. (3.1). These weighted play operators are then summed to form a hysteresis loop, of which an example is shown in Figure 3.4b.

The parameters a_i for $i = 0, 1, 2 \ldots Q$ determine the shape of the hysteresis curve. The shape of this curve is dependent upon the considered actuator and its piezoelectric material. For this reason, these parameters are system specific and must be identified by matching the model with training data obtained from the actuator. This model identification procedure is performed by applying the Differential Evolution [38] algorithm. The model identification and more specifically, the implementation of the Differential Evolution algorithm, are explained in more detail in the next chapter.

3.3 Linear Model: Spring-Damper and Vibration

Next to hysteresis, vibrational dynamics must also be considered when modeling the behaviour of piezo scanning stages. This can be achieved using a linear model, which is demonstrated in previous work such as [1, 16, 32]. In this section, a linear model is formulated for capturing the linear dynamics of the piezo-actuated scanning

stage, including vibrational dynamics. The linear model that describes the vibrational dynamics is defined as G_v. The vibrational dynamics are measured using low voltage amplitude actuation, less than 5% of the full stroke voltage. For this operating region, the amplitude-dependent behaviour resulting from hysteresis is insignificant and negligible [16], resulting in approximately linear behaviour. Note that the amplitude-dependent behaviour for higher driving voltages is captured by the hysteresis model H. In order to quantify a vibrational model G_v that is able to describe the vibrational dynamics specific to the scanning stage, a model identification must be performed using experimental data as well. This is explained in more detail in Chapter 4. Figure 3.5a shows vibration behaviour in the scanning stage.

The experimental results shown in Figure 3.1 show additional low frequency voltage-to-displacement behaviour. The peak-to-peak output displacement is increasing in the low-frequency domain (10-100Hz) as the actuation frequency decreases. This is shown more clearly in Figure 3.5b, where some of the displacement data in Figure 3.1 is shown as a function of normalized time. At low frequency, the dynamics of typical scanning stages are stiffness based, i.e. a flat frequency response is observed, which contradicts with the voltage-to-displacement behaviour observed in Figure 3.1, where a small increase in magnitude is still visible as a function of decreasing actuation frequency. The exact cause of this behaviour is unknown at this point. It is recommended to investigate the root of this behaviour in future research when utilizing the test setup presented in Chapter 2. Despite the fact that creep is not the cause of this behaviour, the viscoelastic spring-damper model G_{SD} [15, 16] still allows for modeling the observed behaviour. This model is defined as

$$G_{SD}(s) := \frac{\hat{y}}{\hat{u}} = \frac{1}{k_0} + \sum_{i=1}^{N_{SD}} \frac{1}{k_i s + c_i}, \tag{3.7}$$

where k_i for $i = 1, 2, \ldots, N_{SD}$ are stiffness coefficients and c_i for $i = 1, 2, \ldots, N_{SD}$ are damping coefficients. The parameter N_{SD} represents the model order of the spring-damper model, also known as the Kelvin-Voight model [16]. As with the unknown parameters within the hysteresis model H, these coefficients are system specific and must be identified through model identification as well, using training data. This is explained in the next chapter, where a motivation for the selected model order N_{SD} is

given as well. The full linear model $G(s)$ is given as

$$G(s) = G_{SD}(s)G_v(s), \tag{3.8}$$

describing the linear dynamics within the system. With this, the full modeling framework that is proposed in this section is shown schematically in Figure 3.3.

3.4 Conclusion

In this chapter, a modeling framework is proposed for characterizing the hysteresis and dynamics of a piezo-actuated high speed scanning stage. The proposed framework aims at capturing both the amplitude-dependent behaviour and the frequency-dependent behaviour within the scanning stage. The proposed framework utilizes a rate-independent Prandtl-Ishlinskii hysteresis model H cascaded with a linear model G, which is used to describe the linear dynamics of the scanning stage. The chapter starts with a motivation for the modeling framework that is chosen, after which each of the sub-models H, G_{SD} and G_v within the modeling framework are formulated and discussed in more detail.

Chapter 4

Model Identification

In the previous chapter, a modeling framework is proposed and formulated to describe the full dynamics of a piezo-actuated high speed scanning stage. In this chapter, the formulated framework is applied to the test setup discussed in Chapter 2. The framework is used to accurately describe the full dynamics of the test setup. For this, a model identification is performed. This is done by identifying the unknown model parameters using model training data obtained from the test setup. This chapter explains the procedure of the model identification of the sub-models H, G_{SD} and G_v. The chapter starts with the identification of the vibrational dynamics G_v by measuring the frequency response of the system. After this, the procedure for identifying the hysteresis model H and the spring-damper model G_{SD} is explained. This is done by applying the Differential Evolution [38] minimization algorithm. This algorithm is explained in detail as well. In the end, the results of the model identification are presented and discussed. The full modeling framework and the corresponding identification procedure is shown schematically in Figure 4.1.

4.1 Vibrational Dynamics Identification

The first step in the identification of the formulated modeling framework is the identification of the vibrational dynamics captured within the linear sub-model G_v. To do so, the frequency response function (FRF) of the scanning stage is measured by exciting the system using white noise. In order to minimize the influence of the hysteresis effect as much as possible, the maximum peak-to-peak input voltage is limited to 2V. The obtained frequency response is shown in Figure 4.2. More details on processing are provided in Appendix A.2. It is clear from the obtained results that two resonance

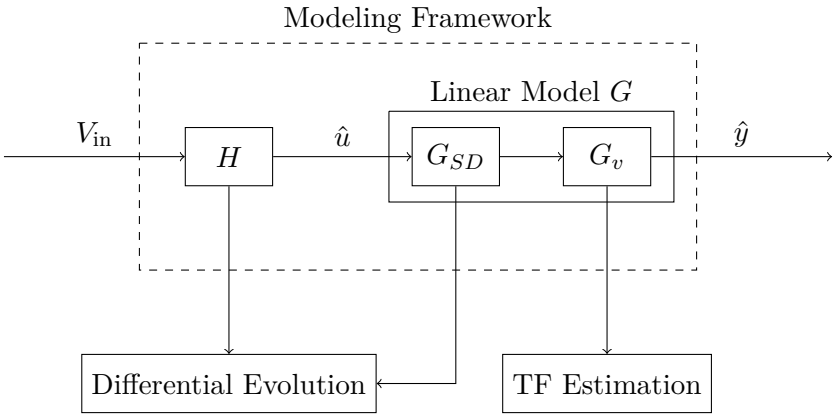

Figure 4.1 Schematic representation of the model identification procedure that is used for each of the sub-models within the formulated modeling framework

peaks are observed within the 0-60kHz frequency domain, located at 24.2kHz and 37.4kHz. A roll-off is observed in the magnitude starting at approximately 3kHz. This is caused by the limited bandwidth of the high voltage amplifier, which is known to be within the order of a few kHz, depending upon the capacitance (210nF) of the piezo and the voltage stroke that is applied. These parameters affect the amount of power and current that must be delivered by the amplifier, which influences its bandwidth. The small signal frequency response of the high voltage amplifier is given in Appendix A.3. Using the frequency response data in Figure 4.2, a model estimation is performed focussing on the 100Hz-45kHz frequency region in order to capture both resonances. The model order is chosen as low as possible while achieving a data estimation fit of at least 75%. The obtained vibrational model G_v is identified in transfer function form. This model is given by

$$G_v(s) = \frac{G_v^{\text{num}}(s)}{G_v^{\text{den}}(s)}, \tag{4.1}$$

in which

$$\begin{aligned} G_v^{\text{num}}(s) &= 2.43 \cdot 10^{29} s^2 + 8.06 \cdot 10^{33} s + 9.10 \cdot 10^{39}, \\ G_v^{\text{den}}(s) &= s^8 + 5.19 \cdot 10^5 s^7 + 2.10 \cdot 10^{11} s^6 + 5.31 \cdot 10^{16} s^5 + 1.18 \cdot 10^{22} s^4 \\ &\quad + 1.61 \cdot 10^{27} s^3 + 1.90 \cdot 10^{32} s^2 + 1.48 \cdot 10^{37} s + 3.74 \cdot 10^{41}. \end{aligned}$$

The obtained transfer function and the frequency response data that is used for the transfer function estimation are both shown in Figure 4.2. The estimated vibrational sub-model G_v contains eight left-half plane poles and is therefore open-loop stable.

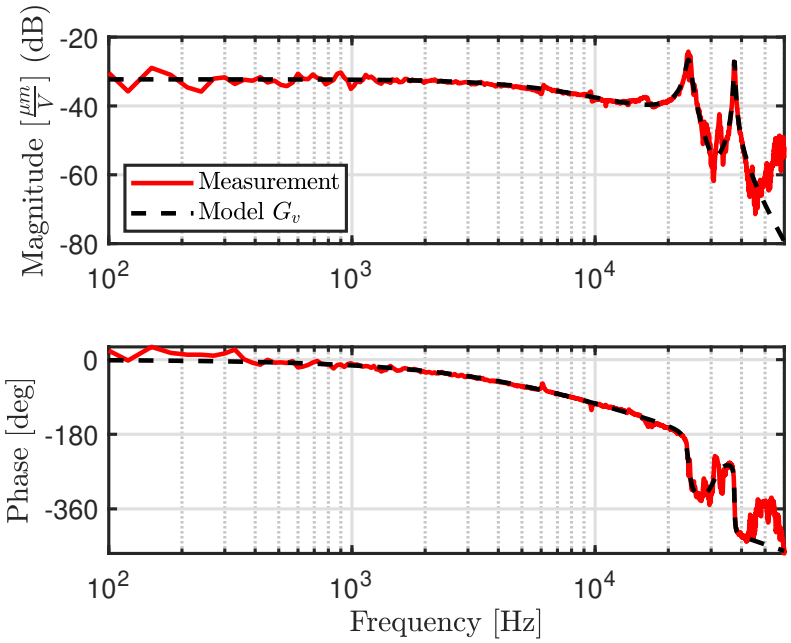

Figure 4.2 Measured frequency response of the scanning stage showing the transfer from input voltage V_{in} to output displacement y and the estimated vibrational model G_v

Furthermore, the estimated model contains two left-half plane zeros, which means its inverse is stable as well. This is favorable for inverse model-based feed-forward control applications [15, 39]. The identified model G_v is used as a fixed model in the identification of H and G_{SD}. This is explained in Section 4.2.

4.2 Hysteresis & Spring-Damper Model Identification

In the previous section, the vibrational dynamics are quantified and captured within the model G_v. With the dynamics identified, the remaining hysteresis and spring-damper models H and G_{SD} can be identified. This procedure is explained in this section. The P-I hysteresis model that is formulated in Eq. (3.5) contains parameters a_i for $i = 0, 1, 2 \ldots Q$ that must be identified in order to quantify the hysteresis model H. Secondly, the spring-damper sub-model G_{SD} formulated in Eq. (3.7) contains parameters k_i and c_i for $i = 1, 2, \ldots, N_{SD}$ which must be identified as well. This is done by minimizing the error between the model output and experimentally obtained training data. In order to quantify this error, an objective function F_{obj} is defined as

$$F_{\text{obj}} = \frac{1}{f} \sum_{i=1}^{f} E_i^{\text{rms}}, \tag{4.2}$$

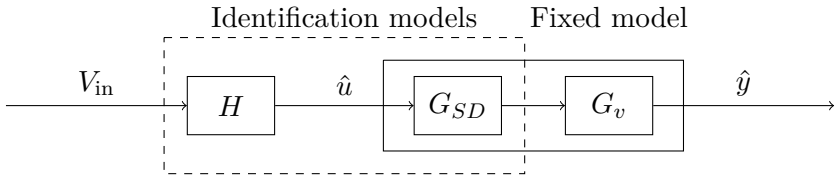

Figure 4.3 Schematic representation of the identification structure for the identification of the hysteresis model H and the spring-damper model G_{SD}, which are cascaded to the already identified vibrational model G_v, given by Eq. (4.1).

where

$$E_i^{\text{rms}} = \sqrt{\frac{1}{n}\sum_{j=1}^{n}\left(\frac{\hat{y}_i(j) - y_i(j)}{\max(y_i) - \min(y_i)}\right)^2}, \tag{4.3}$$

where $y_i(j)$ represents the jth data point of the ith training data set and $\hat{y}_i(j)$ represents the model output corresponding to this data point. Furthermore, E_i^{rms} represents the root-mean-square error (RMSE) of the ith training data set, with respect to the full stroke length.

The identification parameters a_i for $i = 0, 1, 2 \dots Q$ and k_i and c_i for $i = 1, 2, \dots, N_{SD}$ are stored in the parameter vector X:

$$X = \begin{bmatrix} a_0, & \dots, & a_Q, & c_1, & \dots, & c_{N_{SD}}, & k_1, & \dots, & k_{N_{SD}} \end{bmatrix}^\top. \tag{4.4}$$

For each parameter in X, minimum and maximum bounds are defined and stored in $X_{\min}$ and $X_{\max}$, respectively. The parameters in X cannot exceed these bounds during the identification procedure. The model parameters in X are identified by minimizing the objective function F_{obj} in Eq. (4.2), which is equivalent to minimizing the mismatch between the model output and the experimental output. This is equivalent to the following minimization problem:

$$\begin{aligned} \min_X \quad & F_{\text{obj}} \\ \text{s.t.} \quad & X_{\min} \leq X \leq X_{\max}. \end{aligned} \tag{4.5}$$

The hysteresis and spring-damper models H and G_{SD} are cascaded with the previously identified vibrational model G_v given in Eq. (4.1) to obtain the modeled output $\hat{y}$, as shown in Figure 4.3. The output is then used in the objective function F_{obj} in Eq. (4.2).

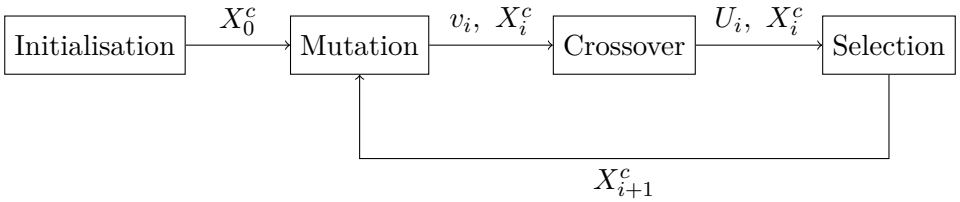

Figure 4.4 Schematic illustration of the Differential Evolution algorithm for a single candidate solution X_i^c at the ith iteration, with the donor vector v_i and the trial solution vector U_i

The Differential Evolution minimization algorithm [38] is applied to solve the minimization problem formulated in Eq. (4.5). This algorithm utilizes a population of candidate solution vectors X^c for $c = 1, 2, \ldots, NP$, where NP represents the amount of candidate solution vectors that are used. Each candidate solution vector represents a potential solution to the minimization problem formulated in Eq. (4.5). These candidate solutions are randomly initialized at the start of the minimization, while meeting prescribed minimum and maximum bounds. An iterative procedure is executed for finding a solution to the minimization problem, consisting of Mutation, Crossover and Selection steps. This is shown schematically in Figure 4.4. These steps are explained in more detail next.

Mutation

Within the Mutation step, a donor vector v_i is defined for a candidate solution vector X_i^c, where i represents the ith iteration of the iterative procedure that being executed. This vector is defined by combing three randomly chosen candidate solution vectors X^{c_1}, X^{c_2}, X^{c_3} as

$$v_i = X_i^{c_1} + f\,(X_i^{c_2} - X_i^{c_3}) \quad \text{with} \quad c_1 \neq c_2 \neq c_3, \tag{4.6}$$

where the mutation factor f is a scalar that is chosen on the interval $[0.4,\ 1]$. Note that there are many other possibilities for defining this donor vector. The work in [38] supports the chosen definition of v_i as given in Eq. (4.6) for the application that is considered in this work. The computed donor vector is used in the Crossover step.

Crossover

Each candidate solution vector is mixed with its corresponding donor vector in order to enhance the potential diversity of the potential solutions. Components of the donor vector and the parameter vector are exchanged and used to create the trial solution

vector U_i. In order to ensure that the constraints

$$X_{\min}(j) \leq X_i^c(j) \leq X_{\max}(j) \quad \text{for} \quad j = 1, 2, \ldots, D$$

on the identification parameters are satisfied, an extra condition is added. Note that D represents the total amount of parameters that must be identified. An entry of the donor vector can only enter the trial vector if it satisfies the constraints on the considered identification parameter. This is made clear in the pseudo-code in Algorithm 1. In this algorithm, Cr is called the crossover rate. This control parameter is used

Algorithm 1 Pseudo-code for trial vector U_i

```
procedure
    for j = 1:D do
        if rand(0,1) ≤ Cr and X_min(j) ≤ v_i(j) ≤ X_max(j) then
            U_i(j) = v_i(j)
        else
            U_i(j) = X_i^c(j)
```

to tune the distribution of X_i^c and v_i in U_i. The defined trial solution vector U_i and its corresponding candidate solution X_i^c are used to evaluate the model using training data.

Selection

In the Selection step, the performance of the new trial solution U_i is compared to the performance of the original candidate solution X_i^c. The full model as shown in Figure 4.3 is evaluated using each of these solutions. The obtained model output $\hat{y}(t)$ is compared to the experimentally measured output $y(t)$ in the objective function in Eq. (4.2). If $F_{\text{obj}}(U_i) \leq F_{\text{obj}}(X_i^c)$, the potential solution has improved by generating the trial vector and the candidate solution vector is updated according to $X_{i+1}^c = U_i$, otherwise, $X_{i+1}^c = X_i^c$. This is an iterative process that is repeated until a pre-specified criterion is met.

It must be noted that when applying Differential Evolution, there is no guarantee of finding a global minimum to the minimization of the objective function in Eq. (4.2). Applying this minimization algorithm most likely results in finding a local minimum.

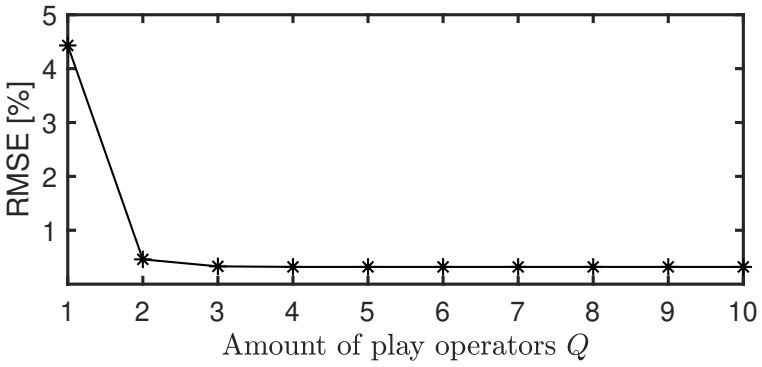

Figure 4.5 Study of the influence of the amount of play operators Q on the achieved modeling accuracy using a 10Hz voltage-to-displacement loop training data set

4.3 Complete Model Identification Results

This section presents and discusses the results that are obtained by applying the identification procedures which were explained in Sections 4.1 and 4.2. The vibrational sub-model G_v is identified as described in Section 4.1. The vibrational sub-model is used in the hysteresis and spring-damper model identification as explained in Section 4.2, where the objective function defined in Eq. (4.2) is minimized by Differential Evolution.

Before the full model is identified, a study is performed in order to determine the amount of play operators Q that is sufficient for modeling the hysteresis nonlinearity. Figure 4.5 shows that using 5 play operators suffices for capturing the hysteresis behaviour, as using more does no longer improve the achieved accuracy.

The 1Hz, 10Hz, 100Hz, and 1000Hz voltage-to-displacement data sets shown in Figure 3.1 are used as model training data sets. During the identification, 600 iterations are performed with 25 candidate solution vectors. Furthermore, the mutation factor is chosen as $f = 0.6$, and the crossover rate is chosen as $Cr = 0.9$. The identification is performed using different spring-damper model orders N_{SD}. The results in Table 4.1 show that using a model order of $N_{SD} = 3$ suffices, as choosing a higher model order does no longer improve the obtained solution. The evolution of the objective function defined in Eq. (4.2) is shown in Appendix A.4. Figure 4.6 shows the training data along with the output $\hat{y}$ predicted by the identified model. The model achieves $< 1\%$ RMS error for each set of training data. The identified parameters of the hysteresis and spring-damper model can be found in Tables 4.2 and 4.3, respectively.

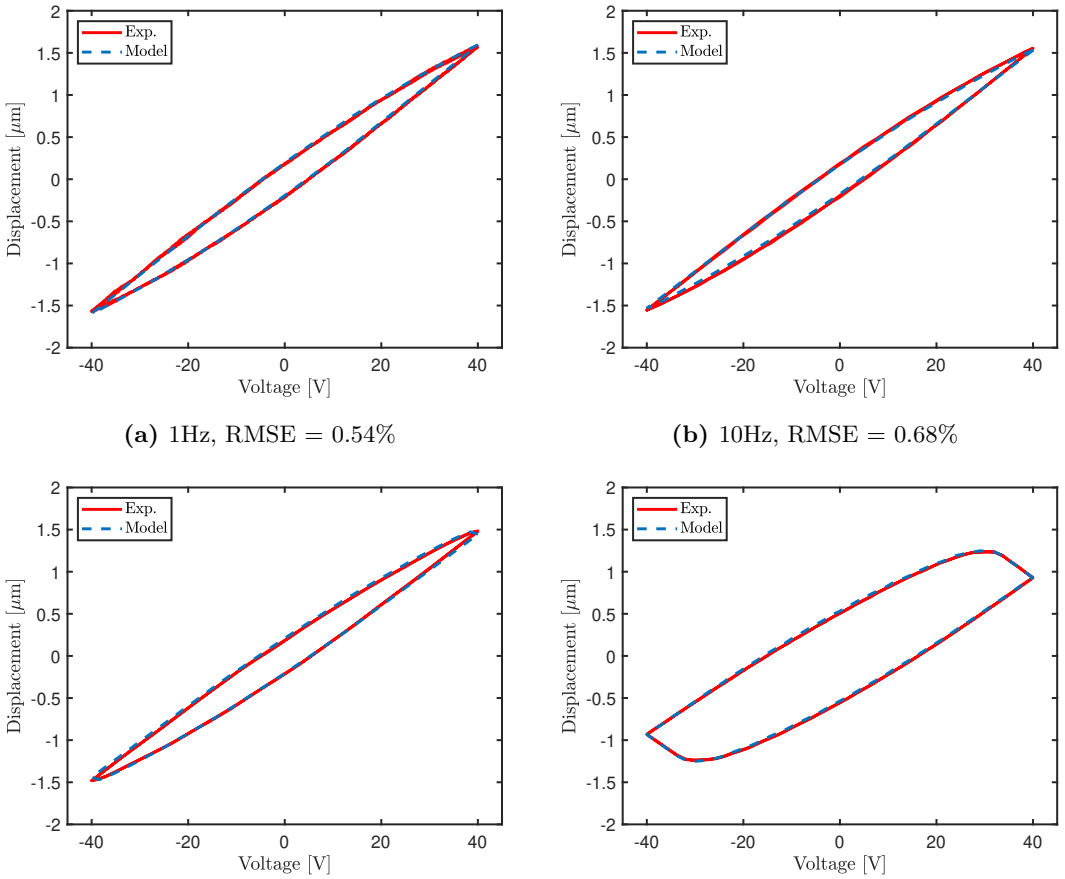

(a) 1Hz, RMSE = 0.54%

(b) 10Hz, RMSE = 0.68%

(c) 100Hz, RMSE = 0.70%

(d) 1000Hz, RMSE = 0.68%

Figure 4.6 Model output $\hat{y}$ predicted by the identified model along with the training data sets that are used for model identification

In Figure 4.7, the bode diagram of the spring-damper model is displayed, which shows an increasing magnitude as the frequency decreases. This coincides with the observed behaviour discussed in Section 3.3. It can be seen that even at high operating frequencies, the identified spring-damper model has some contribution to the dynamics,

Table 4.1 Influence of the spring-damper model order N_{SD} on the minimization of the objective function F_{obj}

N_{SD}	$F_{\textbf{obj}}$
1	0.0090
2	0.0070
3	0.0065
4	0.0065

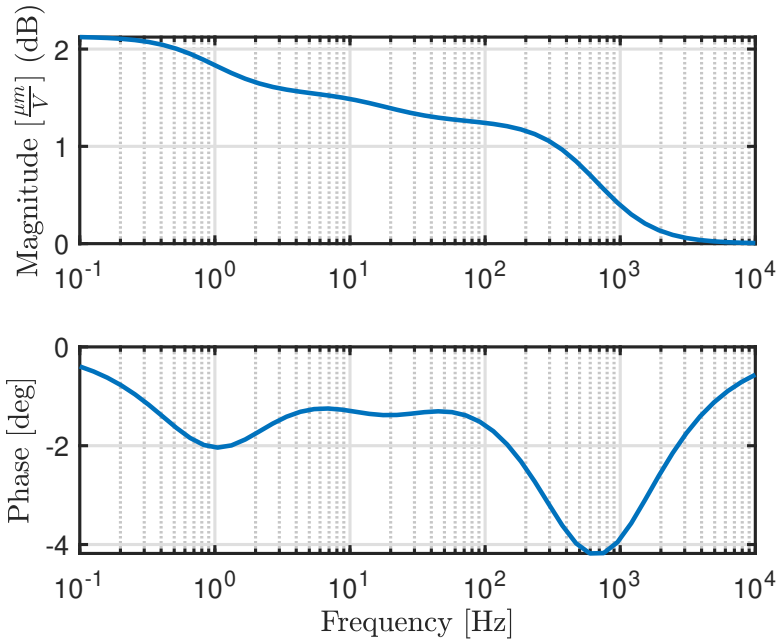

Figure 4.7 Bode diagram of the identified spring-damper model G_{SD}

capturing the dynamics that are not captured in the vibrational model G_v and that cannot be captured within the hysteresis model H. This further confirms that the hysteresis nonlinearity is indeed frequency independent and that all rate-dependent effects can be described using a linear model. With the identification of the vibrational sub-model G_v, the hysteresis model H and the spring-damper sub-model G_{SD}, each of the models within the cascaded modeling framework is identified.

4.4 Conclusion

In Chapter 3, a modeling framework is formulated for modeling the dynamics of piezo-actuated scanning stages, consisting of vibration, hysteresis, and a spring-damper sub-model. This chapter discusses the identification of the modeling framework when applied to the high speed scanning stage in Figure 2.1 by starting with a general overview of the model identification. After this, the identification of each sub-model is

Table 4.2 Identified parameter weights a_i characterizing the P-I model in Eq. (3.5), obtained by applying Differential Evolution

a_0	a_1	a_2	a_3	a_4	a_5
1.1193	0.0730	0.1229	0.0756	0.10227	0.0004

explained in more detail. The vibrational dynamics are quantified by performing FRF measurements. The hysteresis and spring-damper model parameters are quantified by minimizing the modeling error based on training data using the Differential Evolution algorithm. Finally, the results of the full model identification and the identified models are presented and discussed. The identification results demonstrate that the training data can be predicted with less than 1% RMS modeling error.

Table 4.3 Identified parameters c_i and k_i characterizing the spring-damper model in Eq. (3.7), obtained by applying Differential Evolution

c_1	c_2	c_3	k_0	k_1	k_2	k_3
12.0411	6.4210	25.6608	1	1.9502	0.0016	0.2244

Chapter 5

Model Validation

In Chapter 3, a modeling framework for describing the full dynamics of a piezo-actuated high speed scanning stage is formulated. In Chapter 4, the formulated modeling framework is applied to the test setup presented in Chapter 2 by performing a model identification. In this chapter, the identified model is assessed using test data from the setup. This validation focuses on the amplitude and frequency dependent behaviour in the piezo-actuated scanning stage as a result of hysteresis and linear dynamics. Experiments and simulations are performed with pre-computed input voltages $V_{\text{in}}(t)$ that induce amplitude and frequency varying behaviour. These are listed as follows:

1. Fixed Frequency - Fixed Amplitude;
2. Fixed Frequency - Varying Amplitude;
3. Varying Frequency - Fixed Amplitude.

First, the accuracy of the modeling framework is validated for additional voltage-to-displacement loops with constant amplitude measured at different frequencies. This is followed by a validation for voltage-to-displacement loops with varying amplitude. Finally, the modeling accuracy for frequency varying behaviour is validated by using frequency varying input voltages with constant amplitude. For each of the performed validations, the output displacements $\hat{y}(t)$ predicted by the proposed modeling framework are compared to the experimentally obtained output displacements $y(t)$. The model's ability to capture amplitude and frequency varying behaviour is assessed by examining the error signal $e(t)$, which is defined as

$$e(t) = \frac{\hat{y}(t) - y(t)}{\max\left[y(t)\right] - \min\left[y(t)\right]} \cdot 100\%, \tag{5.1}$$

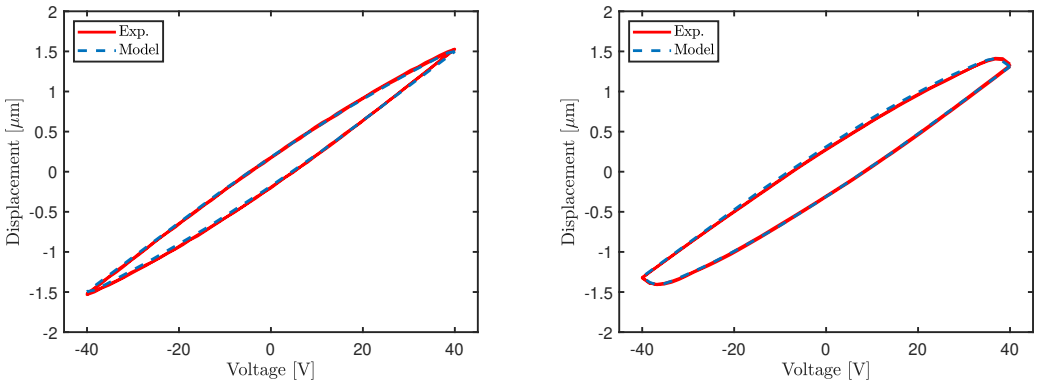

(a) 30Hz, RMSE = 0.64% **(b)** 300Hz, RMSE = 0.73%

Figure 5.1 Measured and modeled output displacement for voltage-to-displacement loops at 30Hz and 300Hz obtained using triangular input voltages

in which the error $e(t)$ is computed in percentage (%), with respect to the maximum peak-to-peak displacement stroke of the test data. Each input voltage is defined as a periodic signal in which a finite amplitude or frequency varying signal element is repeated. With this, the obtained error signals $e(t)$ must be periodic as well. The root-mean-square error (RMSE) of the error signal is examined as well, for which a value less than 1% with respect to the maximum peak-to-peak displacement stroke is desirable. The results are presented and discussed in this chapter.

5.1 Fixed Frequency - Fixed Amplitude

First, the identified modeling framework is validated for triangular input voltages with fixed frequency and amplitude in order to show that the modeling accuracy achieved for model training data is also achieved for test data. The validation is performed for 30Hz and 300Hz voltage-to-displacement loops. The results are shown in Figure 5.1. The results demonstrate the ability of the framework to predict these hysteresis loops with $< 1\%$ RMSE accuracy, which matches the accuracy achieved for the training data as shown in Figure 4.6.

5.2 Fixed Frequency - Varying Amplitude

Next, a validation is performed for an input voltage with varying amplitude, while keeping the frequency of the input voltage constant. With this, the modeling framework's ability to capture the amplitude dependent behaviour as a result of hysteresis is validated. For obtaining test data, two experiments are performed at 100Hz and

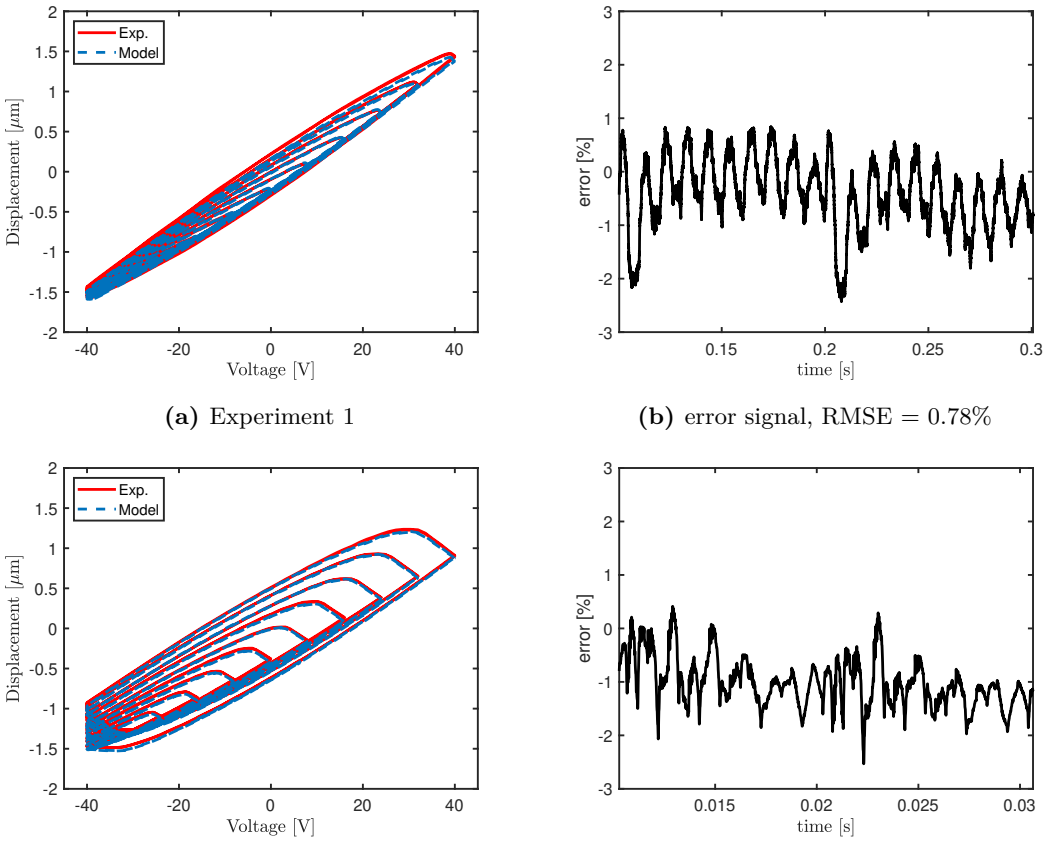

(a) Experiment 1

(b) error signal, RMSE = 0.78%

(c) Experiment 2

(d) error signal, RMSE = 1.12%

Figure 5.2 Measured and modeled output displacements and their corresponding error signals for amplitude varying input voltages at 100Hz and 1000Hz, respectively

1000Hz, respectively. The experimental results and model predictions are compared in Figure 5.2. Additional figures, in which the displacement data in Figures 5.2a and 5.2c is shown as a function of time, are given in Appendix A.5. The results demonstrate that the model is able to accurately capture the amplitude-dependent hysteresis behaviour. The obtained error signals reveal a periodic trend. The RMS error values are comparable to those obtained in the model identification and "Fixed Frequency - Fixed Amplitude" model validation. However, in Figure 5.2d, it can be seen that the error signal of Experiment 2 has a constant offset with respect to zero. The root of this issue lays in the identified spring-damper model G_{SD}, which describes an incorrect creep induced by constant (step) input signals. This offset leads to an RMS error that is slightly above 1%. Solving this issue requires further research. Despite this constant offset, it can be concluded that the Prandtl-Ishlinskii model is able to accurately capture the amplitude-dependent behaviour in the actuator as a result of the hysteresis.

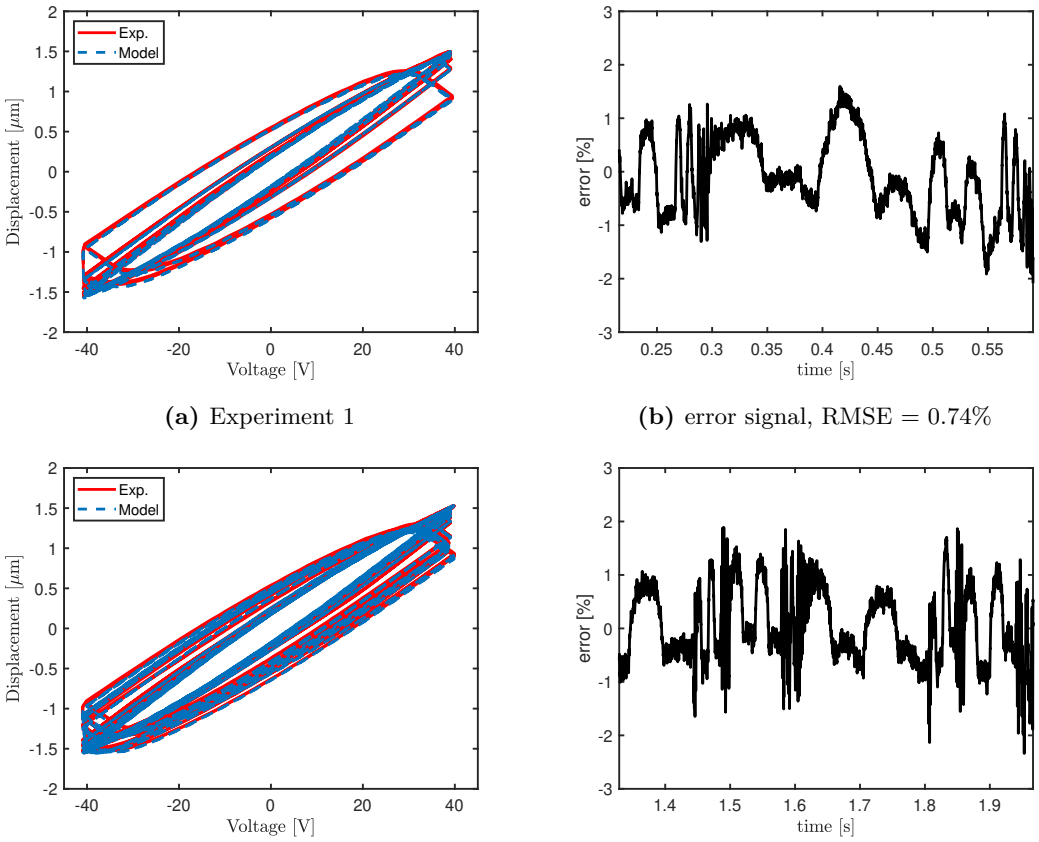

(a) Experiment 1

(b) error signal, RMSE = 0.74%

(c) Experiment 2

(d) error signal, RMSE = 0.68%

Figure 5.3 Measured and modeled output displacements and their corresponding error signals for frequency varying input voltages

5.3 Varying Frequency - Fixed Amplitude

Finally, the modeling framework's ability to capture the rate-dependent behaviour as a result of the linear dynamics is validated. For obtaining test data, two experiments are performed in which triangular input voltages are sent to the scanning stage with varying frequency. In both experiments, the input voltages contain frequencies ranging from 10Hz up-to 1kHz. The experimental results and the model predictions are compared in Figure 5.3. Additional figures, in which the displacement data in Figures 5.3a and 5.3c is shown as a function of time, are given in Appendix A.5. The results reveal a modeling error with a periodic trend as well. Furthermore, the RMS error values are similar (RMSE$<$ 1%) to those obtained in the model identification and previously discussed model validation results. As mentioned previously, this validation considers an operational frequency range of up-to 1kHz. It can be seen that for this frequency range, the magnitude of the modeling error is barely affected by the actuation frequency.

This demonstrates that the rate-dependent behaviour of the scanning stage up-to 1kHz is accurately captured within the proposed modeling framework.

5.4 Conclusion

In this chapter, a model validation is performed for the modeling framework that is formulated and identified in Chapters 3 and 4, respectively. The model validation focuses on the model's ability to capture amplitude-dependent behaviour as a result of hysteresis and frequency-dependent behaviour caused by dynamics up-to 1kHz. The results demonstrate that the model is able to capture and accurately describe varying amplitude and varying frequency characteristics within the stage, with achieving less than 1% RMS error. However, the model validation result in Figure 5.2d does reveal a constant offset in the error signal. The root of this error lays in the spring-damper model G_{SD} and requires more attention in future research. For this, it is advised to properly study the creep effect within the piezo-actuator. This can be done by performing step-response experiments, which reveal the creep effect in the actuator. Furthermore, it is recommended to study the cause of the low-frequency behaviour discussed in Section 3.3 as well. Doing so can provide more insight in the formulation of the linear model G_{SD} in order to prevent the constant offset caused by the model.

Chapter 6

Conclusion

New advancements in nanotechnology applications demand higher bandwidth actuation of piezo scanning stages while maintaining high positioning accuracy. Two of the main bottlenecks in achieving these requirements are hysteresis in the piezo-actuator and vibrational dynamics as a result of the mechanical structure of the scanning stage. In order to overcome these bottlenecks, a framework is required that is able to compensate the hysteresis and vibrational dynamics in such systems at high operating bandwidth. This thesis aimed at formulating a modeling framework that can be used for compensating hysteresis and vibrational dynamics in high speed piezo scanning stages, focussing on amplitude and frequency varying dynamics as a result of hysteresis and dynamics. This work started by examining the rate-dependency of hysteresis loops in a high speed scanning stage. Based on this, a modeling framework is formulated in Chapter 3 that treats hysteresis as a rate-independent nonlinearity. The rate-dependent effects are, along with the vibrational dynamics, described by a linear transfer function model. In the end, the proposed framework consists of two sub-models. A rate-independent hysteresis model and a linear transfer function model, where the linear model is further subdivided into two sub-models, a spring-damper model and a vibrational model.

The proposed modeling framework is applied to a miniaturized high-speed piezo-actuated scanning stage. These stages are used in AFM scan heads for high-speed positioning of the cantilever with respect to the sample during scanning in high-throughput parallel AFM. Chapter 4 explained the identification procedure for quantifying the each of the sub-models within the proposed modeling framework. The identification procedure

started by identifying the vibrational dynamics using FRF measurement data. With the vibrational dynamics identified, the spring-damper model and the rate-independent hysteresis model are identified simultaneously. This is done by utilizing the Differential Evolution algorithm. In the end, the results of the full identification were presented and discussed. The proposed modeling framework achieves $< 1\%$ RMSE for the training data that is used, demonstrating the effectiveness of the proposed framework. Furthermore, this illustrates the suitability of stochastic optimization algorithms such as the Differential Evolution algorithm for the optimization problem that is faced in this chapter.

Finally, the model that is identified in Chapter 4 is assessed using test data in Chapter 5. The validation specifically focussed on the two main dependencies within piezo-actuated scanning stages, which are amplitude-dependency as a result of hysteresis and frequency-dependency caused by dynamics. The validation demonstrates the modeling accuracy that can be achieved using the modeling framework proposed in Chapter 3, which is as low as $< 1\%$ RMS error for both amplitude-dependent and frequency-dependent dynamics up-to 1kHz. However, it must be noted that the spring-damper model can induce an incorrect offset with respect to the test data in some cases. This happens because the spring-damper model is describing an incorrect creep, which is induced by constant (step) input signals. Solving this issue requires additional attention in future research.

Most work in the field of piezo-actuated (high-speed) scanning stages have focused on modeling and compensating either hysteresis or vibrational dynamics in order to improve performance. The result of this work contributes to improved performance at high bandwidth actuation of these systems by developing a modeling framework that allows for predicting the full dynamic behaviour of these systems with high ($< 1\%$ RMSE) accuracy, which includes both hysteresis and vibrational dynamics. The development of this framework opens the door for improved model-based feed-forward control of high-speed scanning stages, and thus for improved performance at high bandwidth operation.

Chapter 7

Future Work

In this thesis, a modeling framework was presented for describing the dynamics of a piezo actuated scanning stage. This framework focusses on amplitude and frequency varying dynamics resulting from hysteresis and linear dynamics. The development of this framework and the execution of the research in this thesis in general has provided new research opportunities. This chapter discusses the most interesting follow up research possibilities.

The work in this thesis provides a modeling framework for high speed scanning stages. Within the framework, the hysteresis and linear dynamics are represented as separate sub-models. For each of these sub-models, a base model or modeling technique was chosen based on the application that is considered in this work. However, for a different application, a different base model or modeling technique may be more suitable. For example, the Prandtl-Ishlinskii hysteresis model can be substituted by a different mathematical model such as the Bouc-Wen model. Alternatively, one can aim for a hysteresis model based on first principle modeling. This also applies to the linear model within the framework. The choice of choosing appropriate models within the proposed framework provides many follow up research possibilities.

The second follow up research that can be done aims at improving the framework itself. It is shown that the rate-dependent hysteresis effects can be explained by additional linear dynamics. These are the result of, among others, the mechanical structure of the stage, the characteristics of the voltage amplification circuit and potentially the creep effect at very low frequency. Properly quantifying the contribution of each of these influences can help in improving the modeling framework, as this can provide

more insight for formulating an appropriate linear model. Furthermore, this can help in improving or choosing the experimental setup's hardware in order to prevent these effects from being present in the first place.

Finally, the framework that is presented is developed for compensating hysteresis and dynamics in high speed scanning stages. This can be done by using feed-forward control combined with feedback control. The framework presented in this work can be implemented in feed-forward control by model inversion. For the Prandtl-Ishlinskii model that is used in this study, an analytical inverse is available that can be directly implemented when the forward model is quantified. Inverting the linear dynamics may result in difficulties as a result of non-causality or non-minimum phase zeros in the system. However, a lot of research within this area is available which can be used to deal with these potential issues. The performance of such a model-based feed-forward implementation based on the proposed modeling framework (combined with feedback control) can be studied in future research.

With this, it is clear that a lot of follow up research can be done based on the results of this thesis. This research can be done by either improving the presented framework itself or by implementation of the presented framework in feed-forward control combined with feedback control.

Bibliography

[1] Santosh Devasia, Evangelos Eleftheriou, and S. O.Reza Moheimani. A survey of control issues in nanopositioning. *IEEE Transactions on Control Systems Technology*, 15(5 SPEC. ISS.):802–823, 2007.

[2] Guo Ying Gu, Li Min Zhu, Chun Yi Su, Han DIng, and Sergej Fatikow. Modeling and control of piezo-actuated nanopositioning stages: A survey. *IEEE Transactions on Automation Science and Engineering*, 13(1):313–332, 2016.

[3] Y. K. Yong, S. O.R. Moheimani, B. J. Kenton, and K. K. Leang. Invited review article: High-speed flexure-guided nanopositioning: Mechanical design and control issues. *Review of Scientific Instruments*, 83(12):p. 121101, 2012.

[4] Toshio Ando, Takayuki Uchihashi, and Noriyuki Kodera. High-Speed Atomic Force Microscopy. *Japanese Journal of Applied Physics*, 51:08KA02, aug 2012.

[5] Hamed Sadeghian, Rodolf Herfst, Jasper Winters, Will Crowcombe, Geerten Kramer, Teun Van Den Dool, and Maarten H. Van Es. Development of a detachable high speed miniature scanning probe microscope for large area substrates inspection. *Review of Scientific Instruments*, 86(11):p. 113706, 2015.

[6] Abu Sebastian, Angeliki Pantazi, S. O. Reza Moheimani, Haris Pozidis, and Evangelos Eleftheriou. Achieving subnanometer precision in a MEMS-based storage device during self-servo write process. *IEEE Transactions on Nanotechnology*, 7(5):586–595, 2008.

[7] Maarten H. van Es, Abbas Mohtashami, Rutger M.T. Thijssen, Daniele Piras, Paul L.M.J. van Neer, and Hamed Sadeghian. Mapping buried nanostructures using subsurface ultrasonic resonance force microscopy. *Ultramicroscopy*, 184:209–216, 2018.

[8] Rodolf Herfst, Bert Dekker, Gert Witvoet, Will Crowcombe, Dorus De Lange, and Hamed Sadeghian. A miniaturized, high frequency mechanical scanner for high speed atomic force microscope using suspension on dynamically determined points. *Review of Scientific Instruments*, 86(11):p. 113703, 2015.

[9] Hamed Sadeghian, Rodolf Herfst, Bert Dekker, Jasper Winters, Tom Bijnagte, and Ramon Rijnbeek. High-throughput atomic force microscopes operating in parallel. *Review of Scientific Instruments*, 88(3):p. 033703, 2017.

[10] Ping Ge and Musa Jouaneh. Tracking control of a piezoceramic actuator. *IEEE Transactions on Control Systems Technology*, 4(3):209–216, 1996.

[11] Babak Mokaberi and Aristides A.G. Requicha. Compensation of scanner creep and hysteresis for AFM nanomanipulation. *IEEE Transactions on Automation Science and Engineering*, 5(2):197–206, 2008.

[12] Vahid Hassani, Tegoeh Tjahjowidodo, and Thanh Nho Do. A survey on hysteresis modeling, identification and control. *Mechanical Systems and Signal Processing*, 49(1-2):209–233, 2014.

[13] M. S. Rana, H. R. Pota, and I. R. Petersen. Improvement in the imaging performance of atomic force microscopy: A survey. *IEEE Transactions on Automation Science and Engineering*, 14(2):1265–1285, 2017.

[14] John A Main and Ephrahim Garcia. Piezoelectric Stack Actuators and Control System Design: Strategies and Pitfalls. *Journal of Guidance, Control, and Dynamics*, 20(3):479–485, may 1997.

[15] D. Croft, G. Shed, and S. Devasia. Creep, hysteresis, and vibration compensation for piezoactuators: Atomic force microscopy application. *Journal of Dynamic Systems, Measurement and Control, Transactions of the ASME*, 123(1):35–43, 2001.

[16] Kam K. Leang, Qingze Zou, and Santosh Devasia. Feedforward Control of Piezoactuators in Atomic Force Microscope Systems: Inversion-based compensation for dynamics and hysteresis. *IEEE Control Systems*, 29(1):70–82, 2009.

[17] Lei Liu, Kok Kiong Tan, Chek Sing Teo, Si Lu Chen, and Tong Heng Lee. Development of an approach toward comprehensive identification of hysteretic

dynamics in piezoelectric actuators. *IEEE Transactions on Control Systems Technology*, 21(5):1834–1845, 2013.

[18] Wei Tech Ang, Pradeep K. Khosla, and Cameron N. Riviere. Feedforward controller with inverse rate-dependent model for piezoelectric actuators in trajectory-tracking applications. *IEEE/ASME Transactions on Mechatronics*, 12(2):134–142, 2007.

[19] Guo Ying Gu and Li Min Zhu. Comparative experiments regarding approaches to feedforward hysteresis compensation for piezoceramic actuators. *Smart Materials and Structures*, 23(9):p. 095029, 2014.

[20] Omar Aljanaideh, Mohammad Al Janaideh, and Micky Rakotondrabe. Enhancement of micro-positioning accuracy of a Piezoelectric positioner by suppressing the rate-dependant hysteresis nonlinearities. *IEEE/ASME International Conference on Advanced Intelligent Mechatronics, AIM*, pages 1683–1688, 2014.

[21] U. X. Tan, T. L. Win, and W. T. Ang. Modeling piezoelectric actuator hysteresis with singularity free prandtl-ishlinskii model. *2006 IEEE International Conference on Robotics and Biomimetics, ROBIO 2006*, pages 251–256, 2006.

[22] Mohammad R. Zakerzadeh and Hassan Sayyaadi. Experimental comparison of some phenomenological hysteresis models in characterizing hysteresis behavior of shape memory alloy actuators. *Journal of Intelligent Material Systems and Structures*, 23(12):1287–1309, 2012.

[23] Klaus Kuhnen. Modeling, identification and compensation of complex hysteretic nonlinearities: A modified prandtl-ishlinskii approach. *European Journal of Control*, 9(4):407–418, 2003.

[24] Mohammed Ismail, Fayçal Ikhouane, and José Rodellar. The hysteresis Bouc-Wen model, a survey. *Archives of Computational Methods in Engineering*, 16(2):161–188, 2009.

[25] Yanfang Liu, Jinjun Shan, Yao Meng, and Dongfang Zhu. Modeling and Identification of Asymmetric Hysteresis in Smart Actuators: A Modified MS Model Approach. *IEEE/ASME Transactions on Mechatronics*, 21(1):38–43, 2016.

[26] T. J. Yeh, Shin Wen Lu, and Ting Ying Wu. Modeling and identification of hysteresis in piezoelectric actuators. *Journal of Dynamic Systems, Measurement and Control, Transactions of the ASME*, 128(2):189–196, 2006.

[27] Mohammad Al Janaideh and Omar Aljanaideh. Further results on open-loop compensation of rate-dependent hysteresis in a magnetostrictive actuator with the Prandtl-Ishlinskii model. *Mechanical Systems and Signal Processing*, 104:835–850, 2018.

[28] Mohammad Al Janaideh, Chun Yi Su, and Subhash Rakheja. Compensation of rate-dependent hysteresis nonlinearities in a piezo micro-positioning stage. *Proceedings - IEEE International Conference on Robotics and Automation*, pages 512–517, 2010.

[29] Wei Li, Xuedong Chen, and Zilong Li. Inverse compensation for hysteresis in piezoelectric actuator using an asymmetric rate-dependent model. *Review of Scientific Instruments*, 84(11):p. 115003, 2013.

[30] Mei Ju Yang, Chun Xia Li, Guo Ying Gu, and Li Min Zhu. Modeling and compensating the dynamic hysteresis of piezoelectric actuators via a modified rate-dependent Prandtl-Ishlinskii model. *Smart Materials and Structures*, 24(12):p. 125006, 2015.

[31] Georg Schitter, Philipp J. Thurner, and Paul K. Hansma. Design and input-shaping control of a novel scanner for high-speed atomic force microscopy. *Mechatronics*, 18(5-6):282–288, 2008.

[32] D. Croft and S. Devasia. Vibration compensation for high speed scanning tunneling microscopy. *Review of Scientific Instruments*, 70(12):4600–4605, 1999.

[33] M. S. Rana, H. R. Pota, and Ian R. Petersen. High-speed AFM image scanning using observer-based MPC-notch control. *IEEE Transactions on Nanotechnology*, 12(2):246–254, 2013.

[34] Sabyasachi Neogi. *Position Control of Nano- Positioning Scanning Stage*. Pdeng mechatronic systems design, Eindhoven University of Technology, 2019.

[35] Hao Jiang, Hongli Ji, Jinhao Qiu, and Yuansheng Chen. A modified prandtl-ishlinskii model for modeling asymmetric hysteresis of piezoelectric actuators. *IEEE*

Transactions on Ultrasonics, Ferroelectrics, and Frequency Control, 57(5):1200–1210, 2010.

[36] Zhiyong Sun, Bo Song, Ning Xi, Ruiguo Yang, Lina Hao, Yongliang Yang, and Liangliang Chen. Asymmetric Hysteresis Modeling and Compensation Approach for Nanomanipulation System Motion Control Considering Working-Range Effect. *IEEE Transactions on Industrial Electronics*, 64(7):5513–5523, 2017.

[37] Guo Ying Gu, Li Min Zhu, and Chun Yi Su. Modeling and compensation of asymmetric Hysteresis nonlinearity for Piezoceramic actuators with a modified Prandtl-Ishlinskii model. *IEEE Transactions on Industrial Electronics*, 61(3):1583–1595, 2014.

[38] Swagatam Das and Ponnuthurai Nagaratnam Suganthan. Differential evolution: A survey of the state-of-the-art. *IEEE Transactions on Evolutionary Computation*, 15(1):4–31, 2011.

[39] John T. Wen and Ben Potsaid. An experimental study of a high performance motion control system. *Proceedings of the American Control Conference*, 6:5158–5163, 2004.

Appendix A

Appendix

A.1 Execution of Experiments

Experiments are performed for the identification of the proposed cascade model, which consists of the hysteresis model H and the linear model G. The general purpose for all experiments is to measure the response in terms of an output displacement of the system for a pre-defined input voltage. The process that is followed during experiments as illustrated in Figure 2.2 can be described as follows:

1. A given input voltage [0-5]V is pre-computed offline.
2. The pre-computed input voltage is loaded to the host PC and sent to the high voltage amplifier, which amplifies the input voltage to a [0-100]V signal.
3. The amplified voltage is applied to the piezo-actuator, which results in a displacement of the actuator.
4. This displacement is being measured by the displacement sensor.
5. Both the displacement data and input voltage (before amplification) are fed back to the host PC via a D/A converter, where it is stored for offline analysis. This minimizes delay between the input and output signals as a result of processing.

These steps are followed for obtaining the required data for performing the model identification. Triangular input signals are used for identifying the hysteresis model. A white noise input signal is used for performing frequency response measurements.

A.2 Frequency Response Measurements

In the frequency response measurement, the output velocity of the stage is measured for a white noise input voltage. This is done because the vibrometer suffers from sensor drift which becomes visible when positioning measurements are performed over longer time periods, which is done for obtaining FRF data. This FRF is shown in Figure A.1.

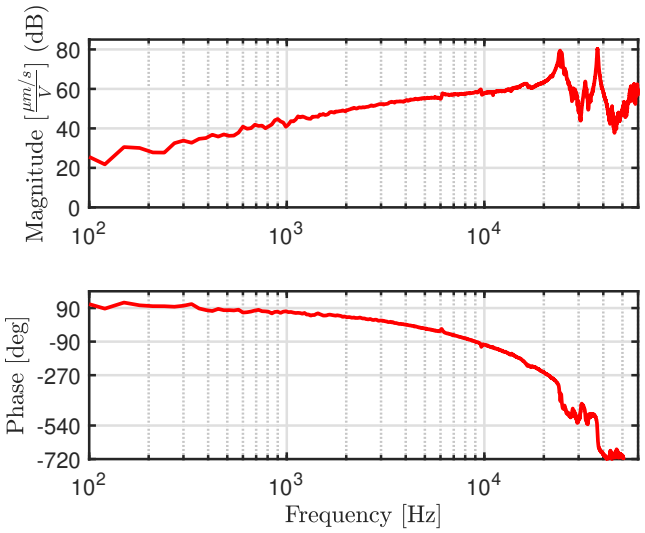

Figure A.1 Frequency response measurement representing the transfer from input voltage to output velocity

The transfer from voltage to displacement is obtained by

$$G_{disp}(j\omega) = \frac{G_{vel}(j\omega)}{j\omega}, \tag{A.1}$$

where ω is the frequency in radians/s. $G_{disp}(j\omega)$ represents the transfer from voltage to displacement and $G_{vel}(j\omega)$ represents the transfer from voltage to velocity.

Additionally, the measured FRF is compensated for $2.5 \cdot 10^{-5}$s of time-delay due to signal processing. The resulting FRF is shown in Figure 4.2.

A.3 High Voltage Amplifier

Figure A.2 shows the small signal frequency response of the high voltage amplifier for different load capacitances. The piezo in the scanning stage has a capacitance of 210nF, which is a limiting factor for the bandwidth of the high voltage amplifier.

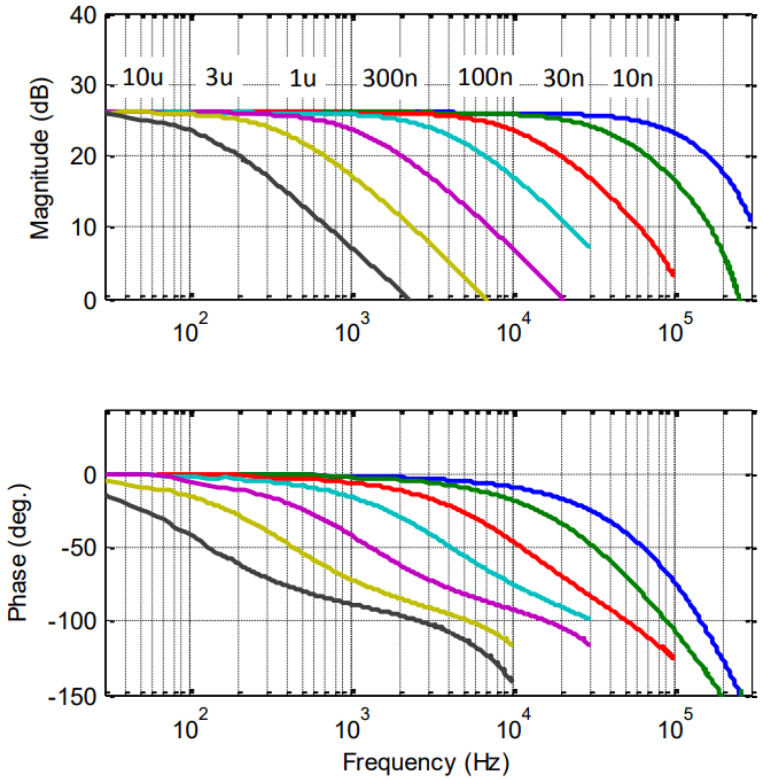

Figure A.2 Small Signal Frequency Response of the high voltage amplifier for different load capacitances, obtained from `www.piezodrive.com`

A.4 Objective Function Evolution

Figure A.3 shows the evolution of the value of the objective function in Eq. (4.2) as a function of the iteration, showing that objective function has converged to a (local) minimum.

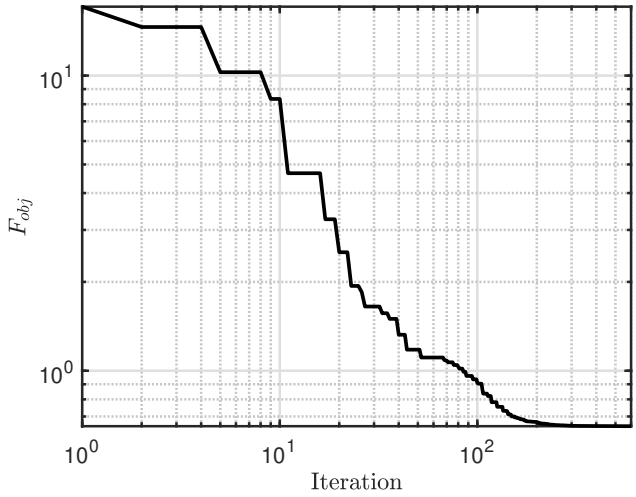

Figure A.3 Evolution of the objective function

A.5 Model Validation: Additional Figures

In this section, the results presented in the model validation in Chapter 5 are shown in time-domain. Figure A.4 shows the varying amplitude trajectories as a function of time and Figure A.5 shows the varying frequency trajectories as a function of time.

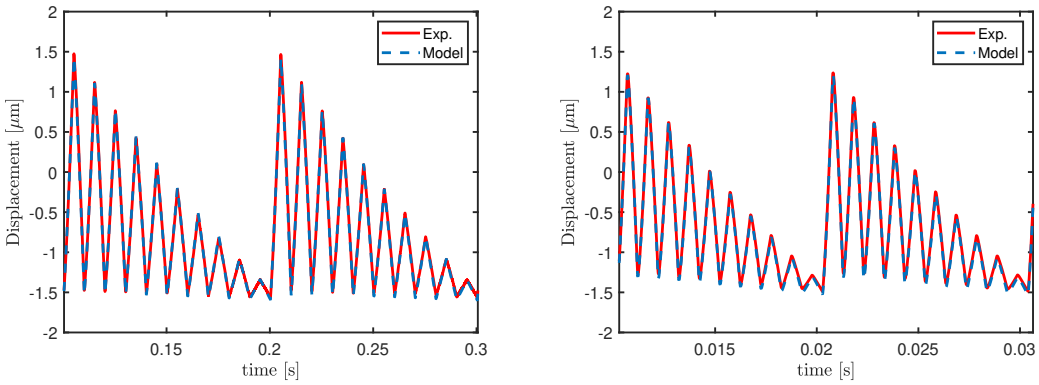

(a) Data of Figure 5.2a shown as a function of time **(b)** Data of Figure 5.2c shown as a function of time

Figure A.4 Measured and modeled output displacement for as a function of time (varying amplitude)

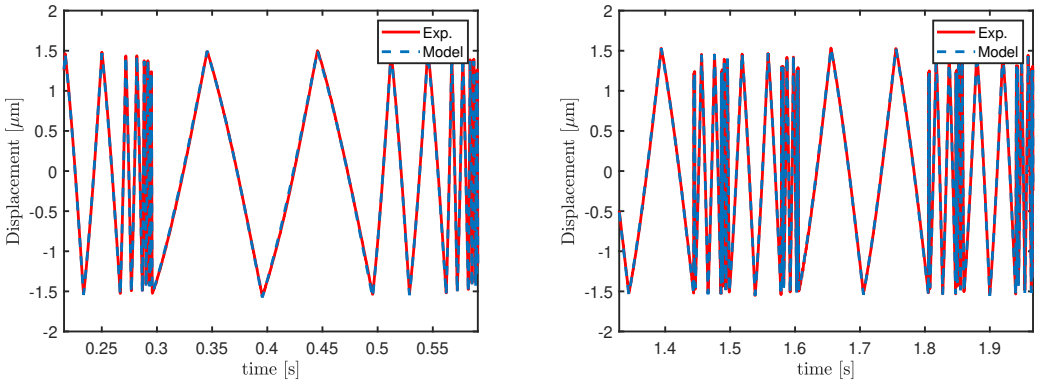

(a) Data of Figure 5.3a shown as a function of time **(b)** Data of Figure 5.3c shown as a function of time

Figure A.5 Measured and modeled output displacement for as a function of time (varying frequency)

Declaration concerning the TU/e Code of Scientific Conduct for the Master's thesis

I have read the TU/e Code of Scientific Conduct[i].

I hereby declare that my Master's thesis has been carried out in accordance with the rules of the TU/e Code of Scientific Conduct

Date

04-06-2020

Name

Aaron Steinbusch

ID-number

0903892

Signature

Aaron Steinbusch

Submit the signed declaration to the student administration of your department.

[i] See: https://www.tue.nl/en/our-university/about-the-university/organization/integrity/scientific-integrity/
The Netherlands Code of Conduct for Scientific Integrity, endorsed by 6 umbrella organizations, including the VSNU, can be found here also. More information about scientific integrity is published on the websites of TU/e and VSNU